ChemComm

FEATURE ARTICLE

View Article Online
View Journal | View Issue

Cite this: *Chem. Commun.*, 2025, **61**, 12097

Multi-metallic nanoparticles: synthesis and their catalytic applications

Yuliang Chen, Ahsan Zohaib, Haobo Sun and Shouheng Sun *

Multi-metallic nanoparticles (MMNPs) have recently garnered significant interest due to their inclusion of different metal atoms within a single nanostructure. The interactions among these metal atoms induce novel properties in MMNPs, making them an ideal platform for exploring the complex interplay between structure and properties, particularly in terms of catalytic properties. This review summarizes recent advancements in the synthesis and catalytic studies of MMNPs. It begins by outlining the synthesis of MMNPs with well-defined structures, including solid solutions, intermetallics, composite core/shell structures, heterodimers, and high-entropy alloys. These MMNPs exhibit unique electronic and surface properties that are crucial for enhancing catalysis. Using representative examples, the review further highlights the promising applications of MMNPs in catalyzing important chemical reactions related to energy conversion and green chemistry, achieving high reaction efficiencies. Finally, the review discusses strategies for attaining atomic precision in the synthesis of MMNPs and optimizing their catalytic performance for a broader range of chemical reactions.

Received 15th March 2025,
Accepted 8th July 2025

DOI: 10.1039/d5cc01468a

rsc.li/chemcomm

1. Introduction

Multi-metallic nanoparticles (MMNPs) discussed in this review are a class of nanomaterials composed of two or more distinct metal elements, forming either well-mixed alloy structures or phase-separated composites. The alloy structures can be further categorized into solid solutions, where different metal atoms randomly occupy positions within the crystal lattice, and intermetallic compounds, where metal atoms are arranged in a chemically ordered manner. In contrast, composite structures include core/shell and heterostructures, in which the constituent metals crystallize independently into distinct structural domains. MMNPs have garnered significant attention in recent years due to their unique structure-induced physical and chemical properties, particularly in catalysis.[1,2] By incorporating multiple elements into a single NP, intermetallic interactions generate synergistic surface environments that facilitate multi-step chemical reactions with enhanced efficiency in both kinetics and energy usage. Moreover, the high degree of structural tunability makes MMNPs a promising platform for investigating structure–catalysis relationships, thereby enabling the rational design of NP parameters to optimize reaction performance.

In this review, we summarize recent advances in the synthesis and catalytic applications of MMNPs. We begin with an overview of synthetic strategies for fabricating MMNPs, including conventional alloys, high-entropy alloys (HEAs), core/shell structures, and heterostructured configurations. Next, we highlight the catalytic roles of these MMNPs in representative reactions, including electrochemical reduction, electrochemical oxidation, and thermochemical processes. Finally, we discuss potential directions aimed at achieving improved control over the synthesis and properties of MMNPs to expand their applicability in catalysis.

MMNPs have recently become a prominent area of study and have been actively reviewed.[2–5] However, these reviews often lack comprehensive coverage of MMNPs and provide limited discussion on NP-composition-dependent catalysis. This current review summarizes a broad range of MMNPs, particularly those studied in the past five years. Specifically, using representative examples, it covers recent advancements in MMNP synthesis and catalytic applications, including both electrocatalysis and thermocatalysis, which are closely related to highly efficient energy conversion and green chemistry.

2. Synthesis of MMNPs

MMNPs can be synthesized using various methods, including solution-phase reactions, laser ablation, and solvothermal techniques. Each method offers distinct advantages and limitations in controlling the NP composition, morphology, and crystal structure.[2] Our focus here is on summarizing solution-phase synthesis. Based on their structural nature, MMNPs can have either a solid solution or an intermetallic structure. In the solid

Department of Chemistry, Brown University, Providence, Rhode Island, 02912, USA. E-mail: ssun@brown.edu

Table 1 Representative examples of MMNPs: synthesis and applications in catalysis

MMNPs	Structure type	Synthetic approach	Synthetic conditions	Applications	Ref.
PtM (M = Co, Fe, Ni)	Solid solution	Co-reduction	Solution phase; reducing agents: super-hydride/polyalcohol/borane; surfactants: trioctyl-phosphine, OAm, OAc	ORR (in 0.1 M $HClO_4$)	7, 18 and 19
PdM (M = Co, Cu)	Solid solution	Co-reduction	Solution phase; reducing agent/surfactant: OAm	FAO (in 0.1 M $HClO_4$ and 2 M HCOOH)	9
RuM (M = Pd, Ni, Cu)	Solid solution	Co-reduction	Solution phase; reducing agents: poly-alcohol/superhydride; surfactants: PVP, OAm, OAc	NO/CO oxidation	14–16
PtCo–M (M = Mn, Fe, Ni, Cu, Zn)	Solid solution/ intermetallic	Co-reduction/ annealing	Solution phase; reducing agent: borane *tert*-butylamine. annealing at 650 °C under 5 vol% H_2/Ar	ORR (in H_2–O_2 fuel cells)	13
PtCo–M (M = Ga, Pb, Sb, Cu)	Solid solution/ intermetallic	Wet impregna-tion, annealing	Solid phase annealing at 1000 °C under 5 vol% H_2/Ar	ORR (in 0.1 M $HClO_4$)	20
B2-CuPd	Intermetallic	Halide-mediated co-reduction	Solution phase; reducing agent and surfactant: OAm	ORR (in 0.1 M $HClO_4$)	40
$L1_0$-PtM/Pt (M = Co, Ni, Fe)	Core/shell	Dealloying	Surface etching in 0.1 M $HClO_4$ and annealing at 400 °C under 5 vol% H_2/Ar	ORR (in 0.1 M $HClO_4$)	19, 49 and 56
Au/MPt (M = Fe, Co, Cu)	Core/shell	Seed-mediated growth	Solution phase; co-reduction of metal precursors and deposition of MPt over seeding Au NPs	MOR (in 0.1 M $HClO_4$ + 0.1 M methanol)	48
Au/Pd NPs dimer	Dimer (Janus)	Polymer-mediated growth	Solution phase; growth of Pd onto Au NPs in amphiphilic block copolymers	—	67
FeCoNiPtRu	Solid solution	Co-reduction	Solution phase; reducing agent: polyalcohol; surfactant: OAm, OAc	—	77
PdCuPtNiCo	Solid solution	Core/shell diffusion	Annealing core/shell CuPd/PtNiCo at 600 °C	ORR (in 0.1 M KOH)	76
PtPdAuFeCoNiCuSn	Intermetallic	Annealing	Annealing HEA NPs at 1000 °C	—	81

OAm: oleylamine; OAc: oleic acid; PVP: polyvinylpyrrolidone; ORR: oxygen reduction reaction; FAO: formic acid oxidation; MOR: methanol oxidation reaction.

solution structure, constituent elements are randomly distributed throughout the crystal network, while in the intermetallic structure, atoms are orderly arranged within the crystal network. Both structural types are considered homogeneous. MMNPs can also form heterogeneous structures, in which atoms are organized in different crystal domains, as shown in core/shell and hetero-dimer structures. In this section, we comment on some common methods that have been explored to synthesize MMNPs, as summarized in Table 1.

2.1. Synthesis of bi-/tri-metallic solid solution MMNPs

In conventional solution-phase synthesis, the formation of MMNPs alloys generally proceeds through sequential nucleation steps, which arise from the varying reduction potentials and/or decomposition chemistry of metal precursors. Solution-phase reduction reactions are frequently employed to synthesize bimetallic or trimetallic solid-solution NPs because they allow for precise control over NP growth conditions, including precursors, reducing agents, ligands, solvents, and reaction temperatures.[6] Under common solution-phase synthetic conditions, solid-solution structured MMNPs are often formed. One widely used method for synthesizing solid-solution alloy NPs is the co-reduction of multiple metal precursors in the presence of a suitable reducing agent, as summarized in Table 1. An early example of this approach is the synthesis of monodisperse FePt NPs *via* the co-reduction of $FeCl_2$ and $Pt(acac)_2$ (acac = acetylacetonate), using lithium triethylborohydride ($LiBEt_3H$, a superhydride) as the reducing agent, and oleic acid and oleylamine as stabilizing ligands.[7] A high-boiling-point dioctyl ether solvent was used to dissolve the precursors, with the assistance of trioctylphosphine, oleic acid, and oleylamine, which formed complexes with the metal ions to facilitate their dissolution. $LiBEt_3H$ solution was then added to reduce both Fe(II) and Pt(II) ions, initiating nucleation and further growth of FePt NPs at the boiling point of the solvent (~292 °C). NP stabilization was achieved through the coordination of oleate ($RCOO^-$) and oleylamine (RNH_2) ligands to the metal surface. This co-reduction method enabled excellent control over particle size, producing NPs as small as 4 nm, and allowed tuning of the Fe/Pt ratio by adjusting the molar ratios of $FeCl_2$ and $Pt(acac)_2$. However, the high reactivity of superhydride can pose challenges for handling and scale-up synthesis. Alternatively, polyalcohols like ethylene glycol were tested as milder reducing agents to initiate reduction reactions. However, their weak reducing power often led to the preferential reduction of noble metal precursors, resulting in noble-metal-rich NPs.[8] To address this issue and enable easier control over NP composition, organic borohydrides such as borane morpholine and borane *tert*-butylamine have been employed as more effective reducing agents in the solution-phase synthesis of MMNPs.[9]

Reductive thermal decomposition is another solution-phase reaction approach to MMNPs. Unlike co-reduction, which relies on metal salts as precursors, this approach involves the reduction and thermal decomposition of organometallic precursors. A well-known example is the synthesis of monodisperse FePt NPs through the combined decomposition of $Fe(CO)_5$ and reduction of $Pt(acac)_2$.[10] This method utilizes

thermally unstable, low-valent metal complexes that decompose swiftly upon heating, releasing metal atoms. This rapid decomposition shortens the nucleation time window, facilitating instantaneous nucleation and promoting the growth of uniform NPs, as demonstrated in the synthesis of Co NPs[11] and Fe NPs[12] *via* the decomposition of $Co_2(CO)_8$ and $Fe(CO)_5$, respectively. Although this method is advantageous for producing monodisperse monometallic and bimetallic NPs, it is quite challenging to achieve the simultaneous decomposition and reduction of different precursors necessary for synthesizing MMNPs.

Solution-phase synthesis requires surfactants to stabilize NPs. However, these surfactants can be challenging to remove, which in turn hinders surface-sensitive catalytic applications. Recently, the solid-phase co-reduction method has emerged as a valuable alternative for synthesizing surfactant-free MMNPs.[13] This method involves wet impregnation of a mixture of metal precursors onto solid supports, typically carbon, followed by high-temperature reaction in a reducing atmosphere (*e.g.*, H_2). In the process, the initial reduction of one metal forms nuclei that act as templates for the subsequent reduction and deposition of other metals. The elevated temperature also enhances atomic diffusion, promoting the formation of solid-solution alloy structures. This solid-phase co-reduction facilitates the large-scale synthesis of supported MMNPs, providing practical advantages over traditional solution-phase methods, especially regarding scalability and surfactant removal. This method has successfully been used to synthesize a wide range of MMNPs with diverse elemental compositions, including RuNi,[14] PdRu,[15] RuCu,[16] RhCu,[17] Pt–M (M = Fe, Co),[18,19] and Pt–Co–M′ NPs (M′ = Fe, Ni, Zn, Cu, Ga, Pb, Sb).[13,20]

In summary, solution-phase co-reduction allows for precise control over NP sizes and compositions, particularly when using strong reducing agents. However, it often leads to compositional inhomogeneity due to varying metal reduction potentials and is prone to surfactant contamination. Reductive thermal decomposition produces highly monodisperse NPs, but its application to MMNPs is constrained by the difficulty of synchronizing precursor decomposition, which can result in phase segregation. The newly demonstrated direct solid-state reaction approach provides a surfactant-free, scalable method for producing supported MMNPs with improved alloying through high-temperature diffusion. The method may evolve as a practical approach to MMNPs if the issue of precise control over NP morphology can be resolved.

2.2. Synthesis of bi- and tri-metallic intermetallic MMNPs

An intermetallic structure is characterized by the ordered arrangement of metal atoms within the crystal lattice. This specific ordering aligns atoms along distinct crystallographic directions, making the structure ideal for examining d–d orbital interactions within each MMNP. These interactions provide enhanced chemical stability of metal components against oxidation and acid etching, compared to a disordered solid solution structure,[21,22] making the structure promising for catalysis under high-temperature and corrosive conditions. However, conventional synthesis methods typically yield solid-solution NPs.[23] These NPs must be annealed at a controlled high temperature to achieve the structural transition from solid-solution to intermetallic. This structural transition is generally governed by the Gibbs free energy change $\Delta G = \Delta H - T\Delta S$, where ΔH is enthalpy, ΔS is entropy, and T is temperature. The process leading to the formation of the ordered structure often has a negative ΔH due to stronger metal–metal bonding interactions associated with structure stabilization, which is also dependent on alloy compositions, and a negative ΔS related to the increase in atom ordering within the structure. This makes T and alloy compositions crucial parameters for promoting atom diffusion within the NP structure and achieving the desired degree of atom ordering.

A common approach to synthesize intermetallic MMNPs is to anneal solid solution MMNPs with the appropriate alloy composition. Fig. 1(a) illustrates the general concept of this annealing-induced ordering process. For instance, intermetallic $L1_0$-PtM NPs (M = Fe,[24] Co,[19,25] Ni,[26] Cu,[27] Zn,[28] Ga,[29] Sn,[30] *etc.*) are typically synthesized by annealing their solid-solution counterparts at 500–900 °C under a H_2/Ar atmosphere.[23] This method has also been extended to the synthesis of trimetallic $L1_0$-PtCoM NPs (M = Fe, Mn, Ni, Cu).[20] A major challenge of this high-temperature annealing is the degradation of NP uniformity due to the surface energy-driven NP mobility, aggregation, and sintering.[22] To mitigate aggregation, the MMNPs are often anchored on stable substrates or coated with stable protective shells (*e.g.*, SiO_2, MgO, and KCl),[28,31–33] as illustrated in Fig. 1(a)-(i). For example, $L1_0$-FePt NPs have been prepared by annealing the MgO-coated FePt NPs. The structural transition occurs within the MgO shell, which is later removed by acid washing, yielding surfactant-free $L1_0$-FePt NPs.[24] Similarly, a stable graphitic carbon shell can be formed by the decomposition of polydopamine around MMNPs to protect their structural transition.[34] The sulfur (S)-doped carbon layer is also found to be effective in suppressing NP sintering.[35]

An alternative approach to stabilize NPs against uncontrolled aggregation during their high-temperature structure transition is to improve atom mobility within NPs. This allows the structural transition to occur at a lower temperature, minimizing the risk of NP aggregation. A common idea is to create defects within the NP structure to facilitate atom diffusion. This is achieved by alloying an atom that cannot integrate with the main structure during the high-temperature annealing process and can subsequently diffuse out of the internal structure, thereby creating defects that promote atomic diffusion, as illustrated in Fig. 1(a)-(ii). This has been applied to prepare various $L1_0$-MMNPs. For example, doping A1–FePt with Au, which has low surface energy and poor miscibility with Fe and Pt, facilitates Fe/Pt ordering at lower temperatures.[24,36] Upon annealing, Au segregates to the NP surface, creating vacancies within the internal structure, lowering the FePt structure transition temperature. Similarly, $L1_0$-FeAgPt NPs are synthesized.[37] Recently, this is further extended to alloying PtM (M = Ni, Co, Fe, Cu, Zn) with a low-melting-point metal M′ (~15%), such as Sn, Ga, or In, to lower the ordering temperature to below 450 °C, enabling the formation of highly ordered $L1_0$-PtMM′ NPs without obvious NP aggregation.[38] Structure

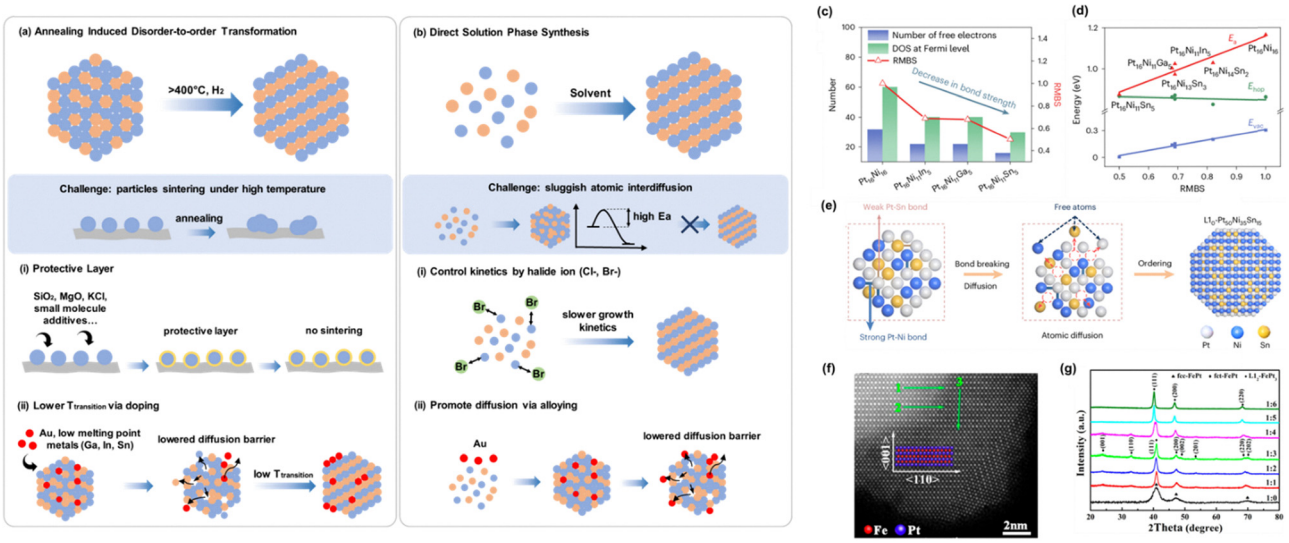

Fig. 1 Summary of (a) annealing-induced disorder-to-order transformation and (b) direct solution phase synthesis of intermetallic MMNPs. (c) The statistic of the number of free electrons, density of states (DOS) at the Fermi level and the relative metal bond strength (RMBS) of different Pt–M–M′ (100) surface. (d) The correlation between E_a (diffusion barrier), E_{vac} (vacancy formation energy), and E_{hop} (hopping barrier energy) and RMBS. (e) Schematic illustration of the promoted ordering process in PtNiSn alloy. Reproduced from ref. 38 with permission from Springer Nature, copyright 2024. (f) The HAADF-STEM images of intermetallic FePt prepared from Cl^- mediated solution synthesis. (g) The X-ray diffraction pattern of FePt under different Pt^{2+} : Cl^- molar ratio. Reproduced from ref. 39 with permission from American Chemical Society, copyright 2018.

studies indicate that M′ weakly binds to Pt or M within the structure (Fig. 1(c)) and can diffuse out easily when the structure is heated, leaving vacancies behind (Fig. 1(d)) and lowering the atom diffusion barrier (Fig. 1(e)). This leads to the formation of intermetallic structure below 450 °C.

Direct solution-phase synthesis has been investigated to produce dispersible intermetallic MMNPs while maintaining their NP shapes. This concept is summarized in Fig. 1(b). For example, intermetallic Pt_3Sn nanocubes were synthesized by co-reducing $PtCl_2$ and $SnCl_2{\cdot}2H_2O$ in 1-octadecene and dodecylamine at 240 °C.[30] However, it is still challenging to extend this method to obtain anisotropic $L1_0$-ordered MMNPs. A more promising approach is to control NP growth kinetics in the presence of a halide ion to form the intermetallic structure, as outlined in Fig. 1(b)-(i). The halide ion (*e.g.*, Br^- or Cl^-) can modulate metal deposition rates by forming strong metal–halide complexes, thereby favoring the formation of stoichiometric intermetallic phases.[39,40] This is nicely demonstrated in the synthesis of $L1_0$-FePt NPs by co-reducing $Fe(acac)_2$ and $Pt(acac)_2$ in the presence of NH_4Cl (Cl^-/Pt^{2+} molar ratio = 3/1).[39] The ordered structure is characterized by both TEM (Fig. 1(f)) and XRD (Fig. 1(g)). Intermetallic B2-CuPd NPs were also prepared by this halide-assisted method by co-reduction of $Cu(acac)_2$ and $PdBr_2$.[40] The ordering can further be achieved directly from the solution phase synthesis condition by incorporating a 3rd metal element in the alloy structure, which lowers the ordering temperature and allows NPs to grow into an intermetallic structure (Fig. 1(b)-(ii)).[41]

2.3. Synthesis of MMNPs with heterostructures

Heterostructured MMNPs consist of distinct crystal domains of metals with well-defined interfaces. Depending on the domain interconnection, they can be classified as core/shell or heterodimer (heterotrimer, *etc.*) NPs. The coexisting components within these NPs frequently interact synergistically, resulting in novel or enhanced properties. For example, linking Au and Cu in the Au–Cu dimer structure greatly enhances their catalytic selectivity for electrochemical CO_2 reduction to multi-carbon products. This improvement is due to synergistic domain interactions between Au and Cu, where CO is produced on Au and then spills over to Cu, where it is further reduced to multi-carbon products.[42] It is now widely accepted that interfaces promote electronic and geometric effects, alter surface adsorption/desorption characteristics,[43] and facilitate charge transfer[44,45] – all crucial for catalytic enhancement. Therefore, precise structural control of heterostructures is essential for optimizing catalytic performance.

Various methods have been developed for preparing core/shell and heterodimer MMNPs.[43,46] The general synthetic ideas are summarized in Fig. 2(a) and (b). Core/shell NPs are commonly synthesized *via* one-pot reaction with controlled NP nucleation and growth kinetics, seed-mediated growth, and dealloying. In one-pot syntheses, metal salts with different reduction potentials are co-reduced, in which the easily reduced metal salt first reacts to form seeding NPs on which the second metal is deposited to form a shell, as demonstrated in the synthesis of core/shell Pd/Pt NPs from the co-reduction of Na_2PdCl_4 and $Pt(acac)_2$.[47] However, in this co-reduction process, it is difficult to prevent concurrent reduction and metal interdiffusion, which often result in NPs with indistinct core/shell boundaries. To prepare a core/shell NP structure with distinct core/shell boundaries, seed-mediated growth is preferred. This method begins with core NPs serving as seeds, around which the shell is grown without separate nucleation

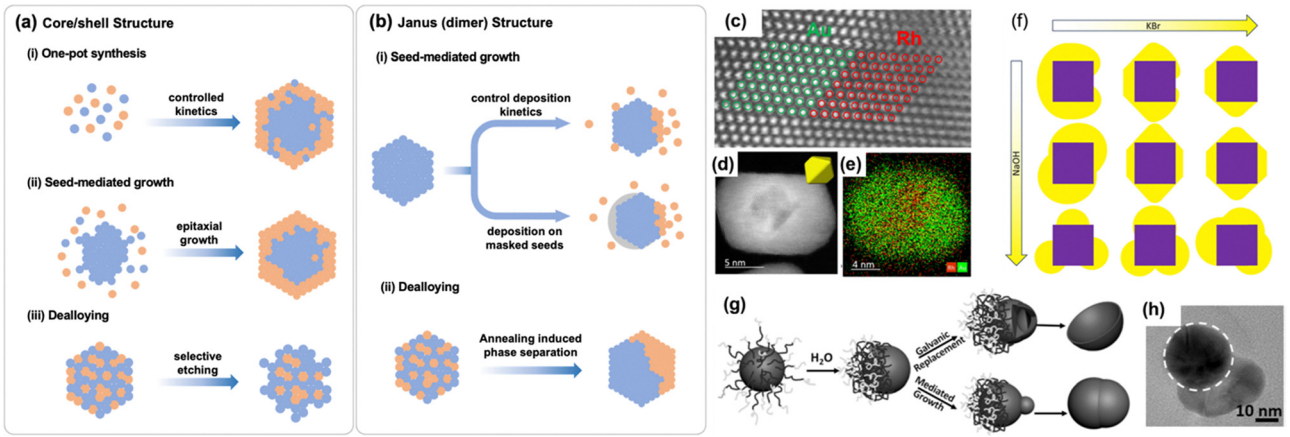

Fig. 2 Summary of the synthetic approaches for (a) core/shell and (b) heterodimer (also called Janus) structures. The HAADF-STEM image of (c) Rh/Au structure with larger lattice distortion, (d) The Rh/Au core/shell NP with the inset showing a model in the same orientation, and (e) the corresponding EDX elemental mapping. (f) The effect of KBr, NaOH concentration on the formation of Rh/Au core/shell structure. Reproduced from ref. 55, licensed under CC BY 4.0.(g) Schematic illustration of the synthesis of dimer structures from amphiphilic-*block*-copolymers capped Au NPs. (h) The TEM image of a typical Au–Pd dimer NPs. Reproduced from ref. 67 with permission from Wiley, copyright 2017.

and growth processes. By precisely controlling the conditions for shell growth, core–shell interdiffusion can be minimized, allowing for better control over shell thickness. For example, Au/MPt (M = Fe, Co, Cu) core/shell NPs were synthesized by depositing MPt onto preformed Au NP seeds under conditions optimized exclusively for the formation of the MPt shell.[48] The lattice mismatch between the core and shell structures can induce lattice strain around the shell,[49] enabling the synthesis of uncommon crystal phases such as the 2H hexagonal phase (AB stacking) as seen in Rh/Ru,[50] Pd/Rh,[51] Au/Cu,[52] and Au/Pd[53] core/shell structures. When lattice mismatch exceeds ~5%, epitaxial growth becomes challenging.[54] Nonetheless, core/shell structures with significant mismatch can still be synthesized by reducing core size and controlling deposition kinetics, as demonstrated in the synthesis of Rh/Au NPs (7.2% mismatch) (Fig. 2(c)–(e)), where 4 nm Rh nanocubes serve as seeds and Au shell is deposited around these seeds by a slow ascorbic acid-induced reduction of $HAuCl_4$. NaOH and KBr may be further added to the reaction solution to control the Au growth kinetics (Fig. 2(f)).[55]

Core/shell NPs can also be synthesized by selectively etching reactive metals from the surface of alloy NPs. For instance, acid treatment of $L1_0$-FePt removes surface Fe, producing a thin (<1 nm) Pt shell.[32] This method has been applied to prepare CoPt/Pt,[19] NiPt/Pt,[56] and CuPt/Pt[49] NPs. As the etching creates surface defects around the shell structure, the core/shell NPs are often annealed at a proper temperature to repair the surface defects and to smooth the shell structure for core stabilization and catalysis studies. The annealing must be carefully controlled to avoid interdiffusion between the core and shell structures.[57]

Unlike core/shell structured MMNPs, heterodimer MMNPs consist of individual NP domains that are attached side-by-side. In solution-phase syntheses, forming heterodimers is challenging when the involved metals have similar atomic sizes, valences, and lattice constants, which favor alloy formation, or when they have highly dissimilar properties, which favor independent nucleation and growth.[58] As a result, the seed-mediated growth method is often employed for the pre-designed growth of new NPs on existing NPs. For example, in the synthesis of Au–Fe_3O_4 and FePt–Fe_3O_4 NPs, Fe is controlled to nucleate asymmetrically on Au or FePt seeds before being oxidized by air to form iron oxide.[59,60] This method has been applied to prepare many other heterostructured NPs.[61,62] Alternatively, heterodimer NPs can be prepared by controlling the deposition kinetics of the second NPs. By slowing the deposition rate, selective growth can be directed toward specific sites on the surface of the core NPs. This approach is demonstrated in the synthesis of Pd–Ag and Pd–Au heterodimers, where slow injection of the Ag (or Au) precursor leads to nucleation on a single facet of Pd nanocubes, forming a dimer structure. Conversely, a faster injection results in uniform deposition over all Pd facets, yielding a core/shell structure.[63,64]

Surfactants anchored on the surface of seeding NPs can significantly influence the deposition of second NPs. This method utilizes the binding affinity of surfactants on different facets of the seeding NPs, permitting new growth only on the facet that is loosely occupied by surfactants, thereby promoting directional growth. In the synthesis of Au–Ag dimers, bifunctional ligands containing both –SH and –COOH groups guided Ag deposition, resulting in an Au sphere–Ag wire dimer structure.[65] Similarly, a polymer mask can be applied to selectively coat the surface of seeding NPs, enabling preferential growth of a new nanostructure, as demonstrated in the synthesis of Au–Pd (Fig. 2(g) and (h)),[66,67] and Au–Ag heterodimers.[68] Annealing-induced phase separation offers another method for forming heterodimers. This approach was used in the synthesis of Pt–Pb dimer NPs by annealing core/shell PtPb/Pt NPs.[69]

2.4. Synthesis of MMNPs of high-entropy alloys

MMNPs containing more than 3 metal components can be viewed as an extension of the alloy structures discussed in

previous sections. However, due to the challenges of incorporating multiple metal elements into a single NP structure and the inherent complexity of these multicomponent systems, these NPs require special attention. In this review, we follow the literature tradition and refer to the MMNPs comprising five or more elements as high-entropy alloy (HEA) NPs.[70] Recently, significant efforts have been focused on developing reliable synthesis strategies for producing HEA NPs.[71,72]

High-temperature pyrolysis is a popular method for producing HEA NPs. This technique involves the rapid pyrolysis of mixed metal precursors using laser, microwave, or electrical heating, followed by quenching to produce NPs with the desired elemental compositions.[71] Plasmonic ablation is employed to fragment bulk HEA materials into isolated NPs.[73,74] Conventional material fabrication techniques like mechanical alloying and electrodeposition are tested, but fail to achieve the desired NP morphology and composition controls. Solution-phase methods developed for bi- and trimetallic NP syntheses have also been adapted for the synthesis of HEA NPs.[75–77] Co-reduction of metal precursors in solution from a non-equilibrium state at elevated temperatures can lead to the formation of 4.7 nm FeCoNiPtRu HEA NPs.[77] However, as the number of constituent elements increases, the complexity of synthesis grows substantially. Variations in reduction potentials, reaction kinetics, and elemental miscibility can cause sequential rather than simultaneous reduction, leading to phase-separated structures.[78] To address this issue, solution-phase synthesis is often combined with solid-state annealing. In this approach, MMNPs are first prepared from solution phase synthesis, and then annealed at high temperatures to promote atomic diffusion into HEA, as demonstrated in the synthesis PdCuPtNiCo HEA NPs from annealing core/shell CuPd/PtNiCo NPs at 600 °C (Fig. 3(a) and (b)).[76] This core/shell design allows sequential incorporation of multiple elements, thus bypassing the need for simultaneous reduction of five elements. This approach has been extended to synthesize other HEA NPs incorporating up to 14 elements.[79] Nevertheless, overcoming the 'mixing' barrier during annealing to form the HEA structure remains a significant challenge. A promising solution is to incorporate a low-melting-point element, such as Ga, which has favorable mixing enthalpies with other metals and provides a strong thermodynamic driving force for homogenization. This has enabled the synthesis of HEA NPs that contain elements of a broad range of atomic radii (1.24–1.97 Å) and melting points (303–3683 K).[80]

Controlled annealing of HEA NPs can induce disorder-to-order transitions, leading to the formation of high-entropy intermetallic (HEI) NPs (Fig. 3(c)).[81] This transformation is highly size-dependent: NPs smaller than 5 nm tend to achieve full ordering, while larger NPs exhibit only partial ordering or form core/shell-like heterostructures (Fig. 3(d)). This highlights the close relationship between structural ordering and high surface energy of NPs. This strategy has been successfully applied to synthesize HEI NPs of PtIrFeCoCu[82] and PtRhFeNiCu.[83]

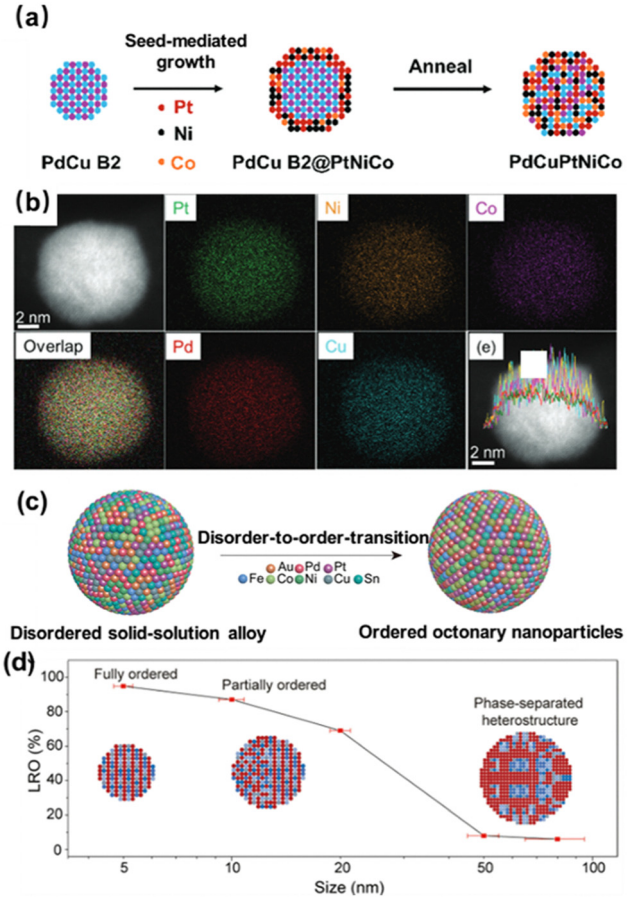

Fig. 3 (a) Scheme of the synthetic process of PdCuPtNiCo HEA NPs. (b) STEM-EDS elemental mapping images of the HEA NP in (a). Reproduced from ref. 76 with permission from Royal Society of Chemistry, copyright 2019. (c) Schematic of the disorder-to-order phase transition from a multi-elemental disordered solid-solution NP to an ordered intermetallic NP. (d) The long-range order (LRO) within the NP as a function of NP size. The insets schematically show the microstructural evolution as a function of the NP size. Reproduced from ref. 81, licensed under CC BY-NC 4.0.

3. Catalytic properties of MMNPs

The integration of multiple metallic components in MMNPs, particularly on their surfaces, leads to unique physical and chemical properties that differ from those of their single-component counterparts.[2,84] This section highlights their catalytic properties.

Catalytic activity is dependent on a catalyst's ability to adsorb and activate reactants, and to desorb products, following the Sabatier principle.[85] MMNPs provide an optimal platform for tuning the electronic structure of active sites to match the activation orbitals of adsorbates, and for designing atomic arrangements that encourage desired binding modes. In MMNPs with fewer than three elements, the electronic structure is mainly influenced by ligand and strain effects, while the ensemble effect dictates the binding configurations of intermediates.[86] To correlate electronic structure with adsorption energy, the d-band center is commonly used as a descriptor: a higher d-band center relative to the Fermi level strengthens adsorption, while a lower center weakens it (Fig. 4(a)).[87]

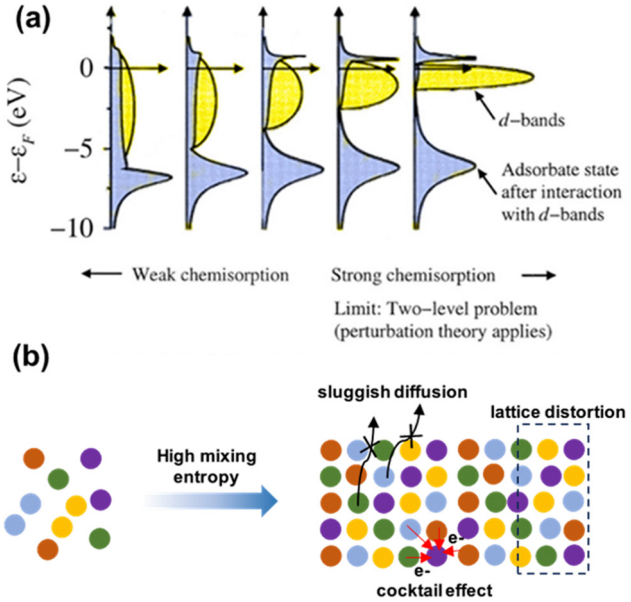

Fig. 4 (a) The local density of state projected onto an adsorbate state interacting with the d bands. Reproduced from ref. 21 with permission from American Chemical Society, copyright 2019. (b) Schematic illustration of the distinct properties of HEA NPs.

The ligand effect arises from electron transfer between surface and subsurface atoms, modifying the d-band center. Lattice mismatch introduces strain: tensile strain narrows the d-band and shifts it upward, enhancing adsorption, while compressive strain has the opposite effect. The ensemble effect, arising from variations in local atomic arrangements, also influences adsorption strength and configuration, thereby affecting catalytic kinetics. HEA NPs, which incorporate a larger number of elements, possess several distinctive features that set them apart from traditional bi- or trimetallic NPs: the high-entropy effect, sluggish diffusion, lattice distortion, and the cocktail effect (Fig. 4(b)).[88] The high-entropy effect, stemming from the mixing entropy of five or more elements, stabilizes the structure, especially under extreme conditions.[89] Sluggish diffusion refers to slower atomic mobility due to varying diffusion barriers and potential energy landscapes, which further enhance phase stability.[90] Lattice distortion, resulting from atomic radius mismatches, introduces tunable strain that can alter catalytic properties.[91,92] The cocktail effect captures the synergistic electronic and structural interactions among the constituent elements, further enhancing performance.[93] With a wide range of surface compositions, HEA NPs offer a spectrum of active sites, each uniquely contributing to overall activity.[94] Collectively, these effects underpin the exceptional catalytic performance and durability of HEA NPs.

4. MMNPs for electrochemical reduction reactions

4.1. Electrochemical CO_2 reduction

The electrochemical CO_2 reduction reaction (CO_2RR) is gaining significant attention as a sustainable route for producing value-added chemicals and renewable energy carriers. NP catalysts are promising for CO_2RR due to their high surface area, abundant active sites, and tunable electronic structure. Depending on catalyst composition and applied reduction potential, CO_2RR can yield single-carbon (C_1) products, such as formate ($HCOO^-$) and carbon monoxide (CO), or multi-carbon (C_{2+}) products like ethylene and ethanol. However, the sluggish initial reduction of CO_2 to HCOO*/COOH*—the rate-determining step—limits the subsequent formation of CO* or CO.[95] Moreover, in aqueous electrolytes, the competing hydrogen evolution reaction (HER) often compromises selectivity. Alloying NPs offers a strategy to improve CO_2 adsorption and activation while suppressing HER.

Noble metal NPs such as Au,[96] Ag,[97] Pd[98] NPs are effective for CO_2RR to CO, which proceeds *via* COOH* stabilization and CO* desorption. However, pure metals exhibit a scaling relationship where stronger COOH* binding can hinder CO desorption or promote HER, thereby reducing overall efficiency.[98] Alloying can break this trade-off by balancing COOH* stabilization and CO* desorption while suppressing HER. For instance, Pd strongly binds CO, impeding its desorption.[98] Alloying Pd with Au downshifts the d-band center, weakening the Pd–CO bond and facilitating CO release at lower overpotentials.[99] Similar improvements are reported for PdAg and PdCu alloys.[100,101] Ternary alloys offer further tunability. PdCuZn nanosheets, for example, exhibit a faradaic efficiency for CO (FE_{CO}) of 96% at −0.35 V (*vs.* RHE), outperforming PdZn (65%) and PdCu (90%) due to a weakened Pd–CO bond that favors linear *CO adsorption over the strongly bound triple-bonded *CO on pure Pd.[102] In Au-based alloys, selectivity gains are less pronounced, but Au_3Cu_1 NPs show a 30% increase in mass activity compared to pure Au.[103] Crystal structure also impacts catalytic performance. Ordered intermetallic AuCu NPs (Fig. 5(a)) enhance CO production while suppressing HER.[104] DFT studies reveal this ordering lowers the activation barrier for COOH* formation and destabilizes H* adsorption, leading to $>80\%$ FE_{CO} (Fig. 5(b)). These intermetallics also exhibit enhanced stability under reaction conditions.[105]

C_{2+} product formation depends on efficient CO coupling, which requires moderate CO binding to ensure adequate surface coverage without inhibiting CO–CO interactions. Cu-based NPs are widely used for this purpose due to optimal CO* binding strength. Alloying Cu with CO-producing metals like Au,[103] Ag,[106] and Ga[107] tunes CO* adsorption and promotes *CO spillover, boosting C_{2+} yields, as demonstrated by CuAu NPs with a low Au content ($\sim$3%).[108] Interestingly, Cu nanorods stained with 2% Au exhibit enhanced selectivity for *n*-propanol (18.2% FE). This improvement is likely due to Au staining on Cu (100) surfaces, which facilitates further CO coupling to the existing C–C coupling intermediates (Fig. 5(c) and (d)).[109]

Core/shell structures or heterodimers are even better catalyst candidates for elective CO_2RR to C_{2+} products. Cu catalysis of the core/shell AgAu/Cu is tuned from a dominant CO product to 77% (FE) C_{2+} products, which is attributed to enhanced CO* adsorption on the Cu shell due to the

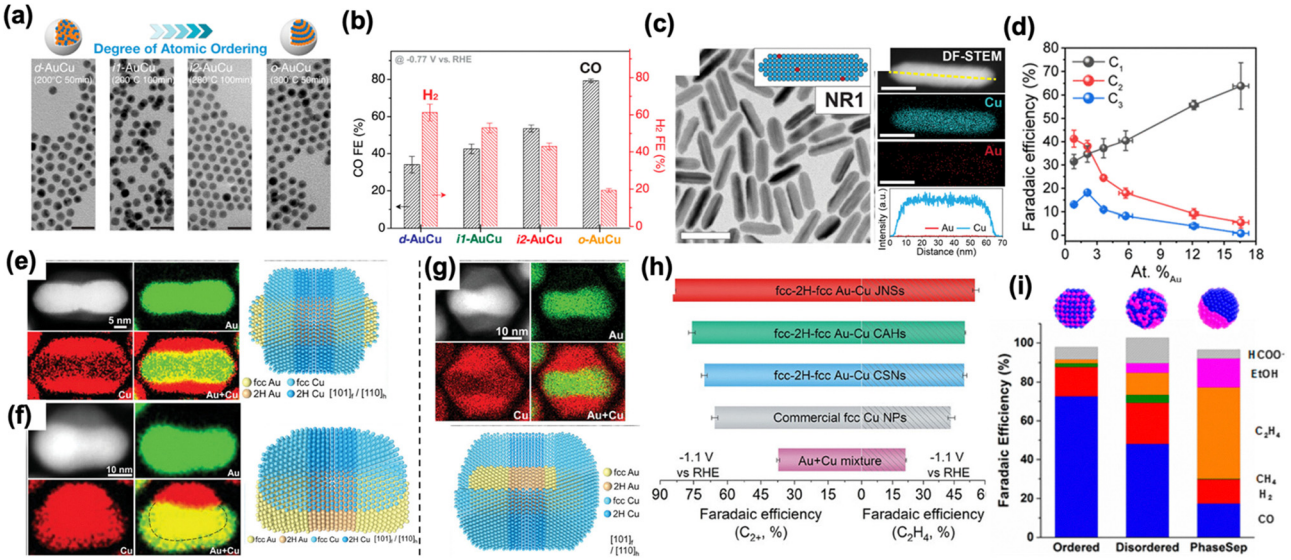

Fig. 5 (a) TEM images showing atomic ordering transformation of AuCu NPs. Scale bar: 20 nm. (b) CO_2RR performance of AuCu NPs with different degrees of ordering (−0.77 V *vs.* RHE, 0.1 M $KHCO_3$ solution) (d: disordered, o: ordered, i1 and i2 are intermediate states). Reproduced from ref. 104 with permission from American Chemical Society, copyright 2017. (c) Cu nanorods (NRs) with surface alloyed with Au. Scale bar: 50 nm (d) The Au-atomic-percentage dependent product distribution in CO_2RR. Reproduced from ref. 109 with permission from American Chemical Society, copyright 2024. (e) Co-axial heterostructured *fcc*-2H-*fcc* Au/Cu. (f) Heterodimer *fcc*-2H-*fcc* Au–Cu structure. (g) Core/shell *fcc*-2H-*fcc* Au/Cu. (h) CO_2RR performance of different heterostructures. JNSs: Janus (heterodimer) structures, CAH: co-axial heterostructures, CSNs: core/shell nanostructures. Reproduced from ref. 52 with permission from Wiley, copyright 2024. (i) Crystal structure and morphology dependent CO_2RR performance of CuPd NPs. Reproduced from ref. 112 with permission from American Chemical Society, copyright 2017.

core-induced shell strain and electronic effects.[110] Crystal structure control in the heterodimers is another important parameter to tune CO_2RR towards C–C coupling products, as demonstrated in 4H- or 2H-structure control of the catalyst in core/shell type Au–Cu heterodimer structures with the C_{2+} products FE reaching 84.3% (Fig. 5(e)–(h)).[52,111] Similarly, heterodimer Pd–Cu or Ag–Cu favors C_{2+} formation.[112–114] As a comparison, the intermetallic PdCu structure is more selective towards C_1 products (Fig. 5(i)). Given the multi-step nature of CO_2RR, catalysts with diverse active sites can accelerate different steps of the reaction. HEA NPs, with their compositional diversity, offer this versatility.[115] Recently, machine learning was applied to model reaction pathways and identify ideal compositions,[116,117] and PdCuAuAgBiIn HEA NPs were found to be active for CO_2RR to formate (98.1% FE).[118]

Stabilizing catalysts for CO_2R remains challenging. Under reaction conditions, NP catalysts tend to undergo structural reconstruction, complicating the correlation between structure and activity. For instance, an initial AgCu alloy NP can disintegrate into smaller Cu- and Ag-rich domains during the reduction process.[119] Numerous designs have been proposed to stabilize Cu-based catalysts, though with limited success. One approach involves alloying Cu with Ga, a more oxophilic metal, to strengthen the Cu bond under reduction conditions and protect it from rapid oxidation.[120]

4.2. Oxygen reduction reaction

The electrocatalytic oxygen reduction reaction (ORR) is a critical process in energy conversion applications such as membrane fuel cells and metal–air batteries. However, its sluggish kinetics hinder practical implementation, necessitating the development of efficient catalysts. Pt-based catalysts remain state-of-the-art, with extensive research dedicated to improving their activity and overcoming kinetic limitations. Theoretical studies and *in situ* experiments suggest that both associative and dissociative mechanisms occur on Pt surfaces, involving multiple oxygenated intermediates (*O, *OH, *OOH) during O_2 reduction.[121,122] Among the Pt catalysts studied, monometallic Pt suffers from strong oxygen adsorption, which limits electron transfer and reduces catalytic activity.[123] Alloying Pt with first-row transition metals such as Co, Fe, and Ni has proven effective in modifying the surface electronic structure and weakening oxygen adsorption, thereby enhancing ORR activity. MMNPs based on Pt alloys, such as PtFe,[18] PtCo,[19] and PtCoNi,[124] have demonstrated impressive improvements in ORR activity compared to commercial Pt/C catalysts. These improvements arise from strain and ligand effects introduced by additional elements: the compressive strain from smaller metal atoms and their electronic interactions with Pt downshift the Pt d-band center, weakening Pt–OH adsorption and accelerating ORR kinetics.[125] This alloying strategy has also been extended to rare-earth metals such as La, Tb, and Tm, which induce pronounced lattice strain and further optimize the adsorption of reaction intermediates, achieving even higher intrinsic activity than alloys with first-row transition metals.[126]

Despite their high activity, Pt-based MMNPs face stability challenges due to oxidation and leaching of non-noble metals under corrosive ORR conditions, particularly in solid-solution

structures. Surface reconstruction and changes in NP size, composition, and morphology can compromise long-term performance.[21] To mitigate these issues, intermetallic Pt-based MMNPs with core/shell architectures, such as CoPt/Pt,[19] PtZn/Pt,[127] and PtFe/Pt,[32] have been developed, exhibiting both superior stability and activity. Strong d–d coupling between Pt and 3d transition metals stabilizes the non-noble components, while the strained Pt shell offers corrosion resistance and boosts catalytic efficiency. For example, $L1_0$-FePt NPs with a Pt shell, synthesized *via* MgO coating, annealing, and acid etching, exhibited exceptional ORR activity and robust stability in acidic media.[32] Similarly, $L1_0$-CoPt NPs with a thin Pt shell (Fig. 6(a) and (b)) retained 95% of their Co content after 24 hours of ORR operation (Fig. 6(c)), whereas their A1-phase (solid-solution) counterparts lost 34% within just 7 hours.[19] $L1_0$-CoPt NPs outperform $L1_0$-FePt/Pt ones for ORR in 0.1 M $HClO_4$ (Fig. 6(d)), likely due to the Co-induced lattice reduction and strong ligand effects. Beyond traditional Pt-transition metal alloys, Pt-dichalcogenide alloys are also promising ORR catalysts. For instance, defective $PtSe_2$ alloys undergo structural reconstruction during long-term ORR operation to form a $PtSe_2$/Pt core/shell structure. This transformation significantly enhances its catalytic performance, achieving a mass activity 4.53 times greater than the commercial Pt catalyst even after 126 000 accelerated durability cycles. The $PtSe_2$ core provides excellent structural stability, while the reconstructed Pt surface maintains high activity.[128]

Incorporating additional elements into MMNPs offers greater flexibility to tune properties and improve ORR stability. As an extension of $L1_0$-CoPt NPs, ternary $L1_0$-CoMPt NPs (M = Mn, Fe, Ni, Cu, Zn) have been investigated both theoretically and experimentally. Intermediates' adsorption was evaluated based on the compatibility of anisotropic strain induced by the Pt surface and the adsorbates. Among the variants, $L1_0$-CoNiPt exhibited the highest ORR activity.[20] Incorporating Rh in the PtRhCu/Pt core/shell structure effectively suppresses Pt dissolution in the ORR process, maintaining excellent stability after 30 000 potential cycles.[129] Further alloying Ti, V, Cr, or Nb with $L1_0$-PtFe NPs can provide electron buffers, suppressing surface polarization of Pt shells under harsh electrochemical conditions (Fig. 6(e)). The $L1_0$-PtFeCr NPs exhibited only a 2.5% drop in mass activity and a 2.9% loss in electrochemically active surface area after 30 000 accelerated durability tests (ADT), compared favorably to $L1_0$-PtFe (3.5% loss in mass activity

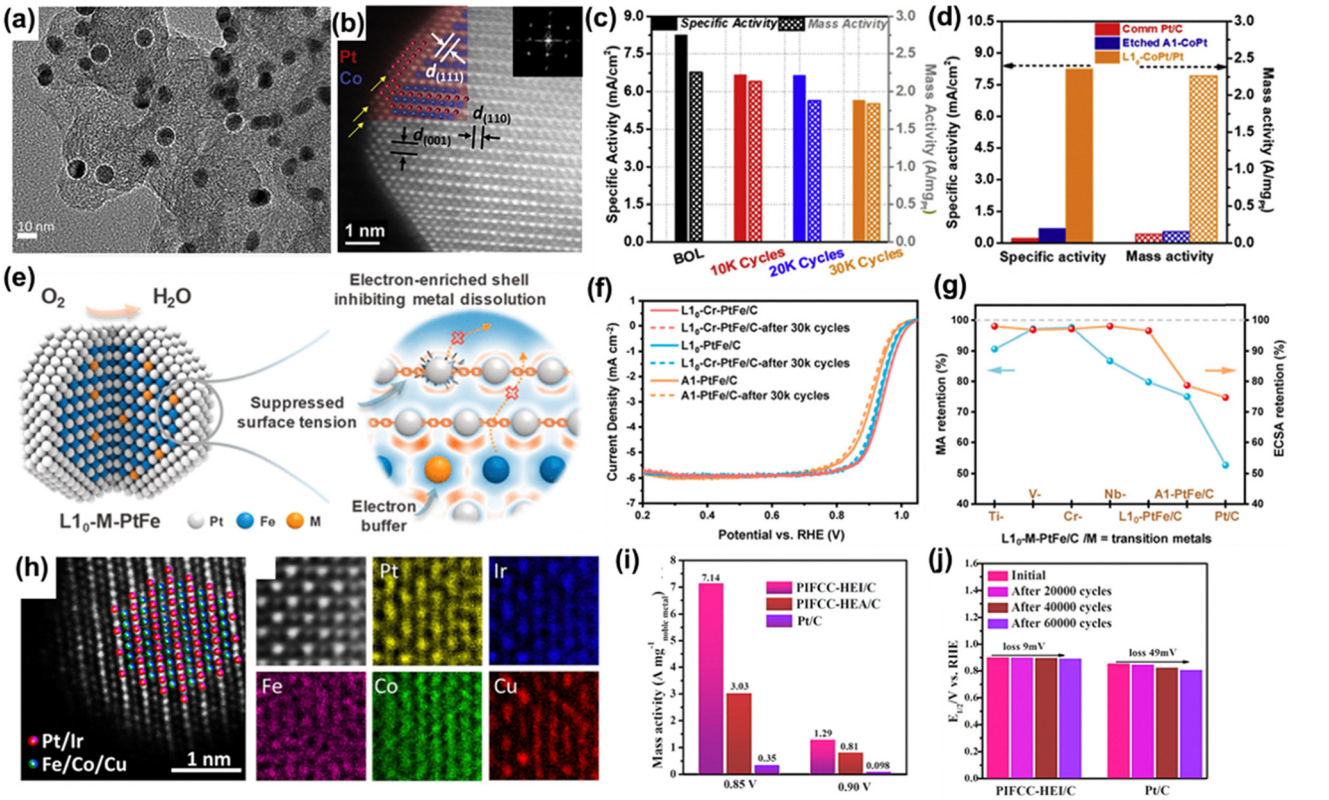

Fig. 6 (a) TEM image of $L1_0$-CoPt/Pt NPs. (b) HAADF-STEM image of $L1_0$-CoPt with a thin Pt shell. (c) The retention of mass & specific activity of $L1_0$-CoPt/Pt in the ADT test. (d) The activity comparison of commercial Pt, etched A1-CoPt, and $L1_0$-CoPt/Pt. Reproduced from ref. 19 with permission from Elsevier Inc, copyright 2018. (e) Schematic illustration of Cr doping as an electron buffer to stabilize $L1_0$-PtFe NPs. (f) ORR LSV polarization curve of the PtFe and PtFeCr catalysts. (g) Retention in mass activity and electrochemical active surface area (ECSA) after ADT test with $L1_0$-M-PtFe. Reproduced from ref. 130 with permission from American Chemical Society, copyright 2024. (h) HAADF-STEM of PtIrFeCoCu (PIFCC) HEI NPs and the corresponding EDX mapping. (i) ORR performance comparison of the HEA NP and commercial Pt catalysts. (j) Shift in half-wave potential ($E_{1/2}$) after ADT test with PIFCC HEI NPs. Reproduced from ref. 82 with permission from American Chemical Society, copyright 2023.

and 21.2% losses in surface area) (Fig. 6(f)). Alloying with Ti, V, or Nb also resulted in higher mass activity retention after ADT (Fig. 6(g)).[130]

HEI NPs are being explored as next-generation ORR catalysts due to their tunable electronic structures and excellent robustness. For example, HEI PtFeCoNiCu NPs demonstrated a mass activity 15.8 times that of commercial Pt.[131] HEI PtIrFeCoCu NPs (Fig. 6(h)) achieved an even higher mass activity of 7.14 A mg^{-1} noble metal at −0.85 V, compared to 3.63 A mg^{-1} noble metal for the corresponding HEA counterpart (Fig. 6(i)). Importantly, these HEI NPs retained 99% of their activity after 80 hours of continuous operation, with only a 9 mV shift in half-wave potential (Fig. 6(j)). Their outstanding performance is attributed to a unique (001) surface that enhances Pt-heteroatom interactions and significantly lowers the d-band center, thereby optimizing oxygen adsorption.[82] Recent theoretical studies suggest that non-Pt elements in HEI NPs may also participate in the four-electron ORR pathway by facilitating O–O bond cleavage in *OOH intermediates.[94] However, this mechanism remains speculative, given that non-noble metals are unstable under acidic ORR conditions. Machine learning has increasingly been employed to design HEI catalysts by optimizing surface strain and formation energy. For instance, computational predictions identified $Pt(FeCoNiCu)_3$ as an optimal candidate, which was experimentally validated to exhibit superior ORR performance (4.09 A mg^{-1} Pt) compared to $PtCu_3$ (0.96 A mg^{-1} Pt), $Pt(CoCu)_3$ (1.77 A mg^{-1} Pt), and $Pt(FeCoCu)_3$ (3.98 A mg^{-1} Pt).[132] The enhanced specific activity of $Pt(FeCoNiCu)_3$ correlates strongly with optimized surface strain, while its excellent stability stems from sluggish diffusion of non-Pt atoms, which increases the alloy's formation energy. These advancements underscore the growing potential of MMNPs for practical ORR applications. Continued efforts in multi-metallic catalyst design, aided by computational modeling and machine learning, are expected to further improve catalytic activity and durability, bringing ORR catalysts closer to commercial viability.

5. MMNPs for electrochemical oxidation reaction

5.1. Alcohol oxidation reaction

The alcohol oxidation reaction (AOR) is widely applied in organic synthesis, energy conversion and storage, and fuel cells. Among these, direct alcohol fuel cells are particularly attractive due to alcohols' high energy density and ease of storage and transport. Common alcohols such as methanol, ethanol, and ethylene glycol undergo direct oxidation in fuel cells to generate electricity. This energy conversion efficiency is critically dependent on Pt- or Pd-based catalysts.[133]

During the AOR, for example, methanol oxidation reaction (MOR), CO-based intermediates frequently form and can poison the catalyst due to the strong binding between Pt (Pd) and CO.[134] Alloying Pt or Pd with oxophilic elements such as Fe, Co, Ni, Cu, Ru, or Sn helps remove oxygenated intermediates from active sites, thereby mitigating the detrimental CO effects.[135–137] Nevertheless, the catalysis remains sluggish due to the additional dehydrogenation steps required to break the C–H bonds.[138] Recent studies have shown that MMNPs can overcome these issues and accelerate MOR kinetics. For instance, $Pt_{18}Ni_{26}Fe_{15}Co_{14}Cu_{27}$ HEA NPs (Fig. 7(a)) show exceptional mass activity (15.04 A mg^{-1} Pt) in catalyzing MOR (Fig. 7(b)).[139]

Density functional theory (DFT) calculations reveal that Co and Ni 3d orbitals contribute to electron depletion, while Cu, Fe, and Co 3d orbitals enhance electron transfer (Fig. 7(c)), thereby facilitating oxidation steps. This synergy underscores the critical role of multi-metallic composition in MOR catalysis.

Ethanol, with its lower toxicity and higher energy density compared to methanol, is another promising fuel. However, its oxidation involves more complex C–C bond cleavage and multi-step dehydrogenation, making complete conversion to CO_2 challenging. It is now generally believed that the ethanol oxidation reaction (EOR) proceeds *via* three main pathways: (i) the direct C_1 ($12e^-$) pathway, where ethanol undergoes full oxidation to CO_2 *via* C–C bond cleavage without forming CO; (ii) the indirect C_1 ($12e^-$) pathway, in which ethanol partially dehydrogenates, forming CO intermediates before they are oxidized to CO_2; and (iii) the C_2 ($4e^-$) pathway, where ethanol is oxidized to acetate without C–C cleavage. Although Pt and Pd are widely used for EOR, they suffer from poor selectivity and catalyst poisoning due to sluggish C–C cleavage.[133] The removal of poisonous species requires *OH involvement, which is difficult to achieve on Pd or Pt surfaces.[140] Alloying with oxophilic metals improves *OH adsorption and CO tolerance, but often favors the C_2 pathway.[141,142] To enhance C–C cleavage, alloying Pt or Pd with Au,[143] Ag,[144] Rh,[145] and Ir[146] has been extensively studied. While Au itself is inactive for EOR, Au-rich PdAu NPs (Au : Pd = 66 : 34) (Fig. 7(d)) can show high mass activity of 19.5 A mg^{-1} Pd in 1 M KOH + 1 M EtOH (Fig. 7(e)), favoring the C_1 pathway (Fig. 7(f)). This enhancement is attributed to the optimized Pd–Pd bond length and electron transfer from Pd to Au, which weakens CO adsorption.[143] The modulation of Pd sites is further demonstrated in core/shell *fcc*-2H/*fcc* Au/Pd nanorods, which exhibit enhanced EOR catalysis with superior mass activity (6.82 A mg^{-1} Pd) and specific activity (13.77 mA cm^{-2}Pd).[53] The epitaxial growth of the Pd shell on Au induces Pd lattice expansion, which promotes *OH adsorption and facilitates complete ethanol oxidation. Furthermore, undercoordinated Pt sites along ultrathin (2 nm) Au nanowires (NWs) (Fig. 7(g) nad (h)) are found to be highly active for C–C bond cleavage *via* the direct C_1 pathway (Fig. 7(i)), demonstrating an unprecedented mass activity of 196.9 A mg^{-1} Pt (Fig. 7(j)).[147] The structure is generally active for catalyzing the primary alcohol, including methanol, ethanol, and *n*-propanol. In another example, core/shell structured Au/PtIr NPs with a stretched PtIr shell exhibit improved ethanol dissociation and C_1 intermediate dehydrogenation. Without the Au core, the PtIr alloy favors the indirect pathway, leading to CO formation and catalyst deactivation.[148]

Stability is a major concern for alloy catalysts under oxidative conditions, particularly in acidic media. To address this

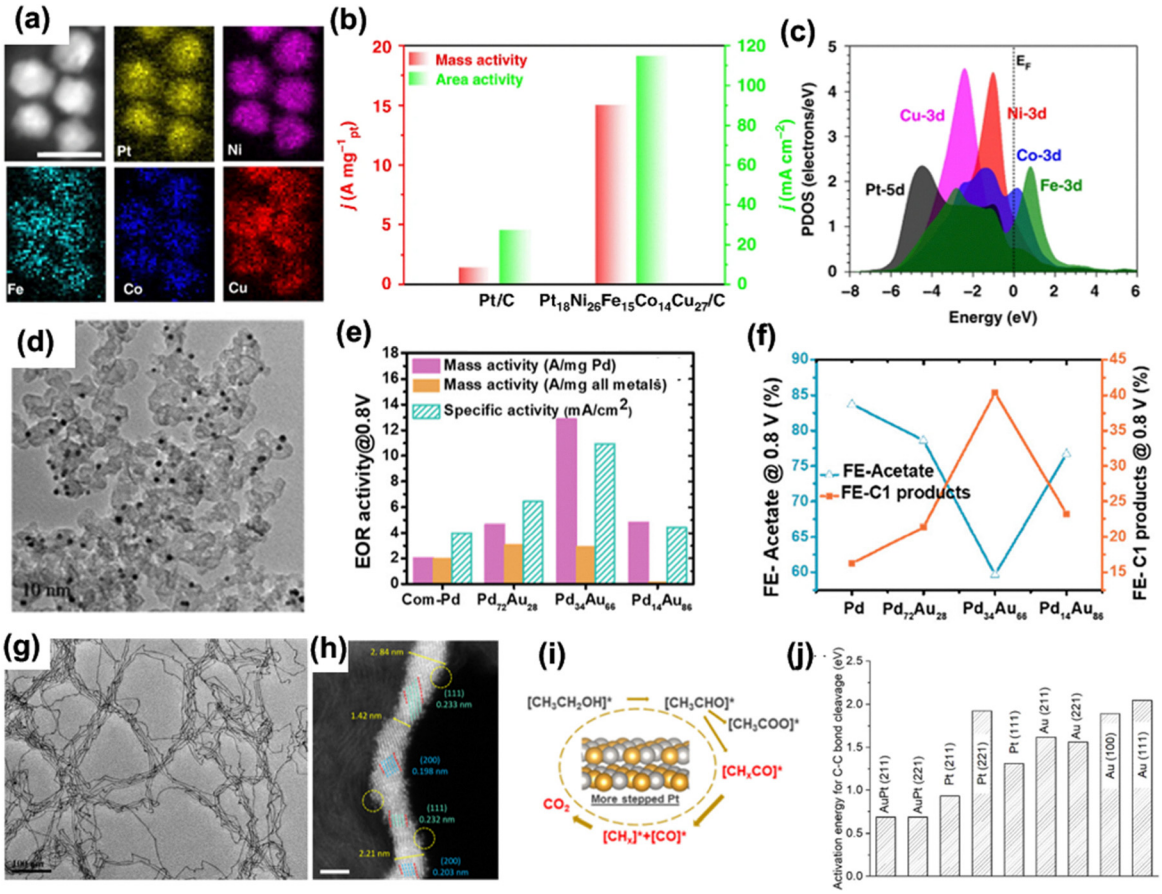

Fig. 7 (a) TEM image and the corresponding EDX mapping of $Pt_{18}Ni_{26}Fe_{15}Co_{14}Cu_{27}$ NPs (scale bar, 5 nm). (b) MOR performance of the HEA NP and commercial Pt catalysts. (c) The PDOSs of the $Pt_{18}Ni_{26}Fe_{15}Co_{14}Cu_{27}$ HEA NPs. Reproduced from ref. 139 with permission from Springer Nature, copyright 2020. (d) TEM image of PdAu NPs. (e) Composition-dependent mass activity of PdAu NPs in EOR. (f) Composition-dependent products selectivity of PdAu NPs. Reproduced from ref. 143 with permission from American Chemical Society, copyright 2019. (g) TEM image of Au/Pt nanowires. (h) High resolution TEM of an Au/Pt nanowire, showing the stepped surface. Scale bar: 2 nm. (i) Schematic illustration of promoted C–C cleavage in EOR on Au/Pt step sites. (j) DFT calculations on activation energy of C–C bond cleavage on different Pt, Au and AuPt facets. Reproduced from ref. 147 with permission from American Chemical Society, copyright 2023.

issue, intermetallic $L1_0$-PtCoAu NPs were introduced as a stable catalyst for AOR in 0.1 M $HClO_4$. The catalyst has a mass activity of 1.55 A mg^{-1} Pt (*vs.* 0.45 A mg^{-1} Pt for Pt/C) and retains its high performance with only a 1.6% loss after 10 000 potential cycles, demonstrating much improved stability than the commercial PtRu NP catalyst (52.4% drop after the same potential cycling).[149] The enhanced performance is attributed to the stable $L1_0$-PtCo core and the CO-resistant AuPt alloy shell.

HEA MMNPs composed of Ir, Os, Pd, Pt, Rh, and Ru were also found to favor the C_1 pathway and deliver record-high EOR activity.[150] Incorporating oxophilic elements such as Fe, Ni, and Cu into the HEA NPs further promotes *OH adsorption and C–C cleavage, as demonstrated by PtRhFeNiCu NPs with excellent CO tolerance.[83] Similar improvements in EOR catalysis have been observed in 15-element HEA NPs.[151] However, it is extremely difficult to unravel the specific roles these metals play in the catalysis. Given that intermetallic structures are significantly more robust than solid solution structures, HEI NPs are expected to be more promising catalysts for EOR. Indeed, a recent study shows that HEI PtPdAuFeCoNiCuSn NPs outperform their HEA counterparts in both activity and stability.[152]

5.2. Oxygen evolution reaction

The oxygen evolution reaction (OER), a critical half-reaction in water splitting and metal–air batteries, involves the oxidation of water molecules to generate oxygen gas.[116] Like the ORR, OER also suffers from sluggish kinetics due to its complex four-electron oxidation process. Noble metals such as Ir and Ru,[153] along with first-row transition metals like Co, Ni, and Fe,[154,155] and their corresponding oxides and hydroxides[156] have been studied as effective OER catalysts. OER typically follows two mechanistic pathways: the adsorbate evolution mechanism (AEM) and the lattice oxygen-mediated mechanism (LOM). In the AEM, the reaction advances through sequential oxidation steps involving surface-bound intermediates such as *OH, *O, and *OOH. The catalytic activity is determined by the

adsorption energies of these intermediates, which must be precisely balanced—excessively strong or weak binding can impede the reaction rate. Various MMNPs have been studied to optimize these adsorption energies in line with the d-band theory. For example, $Ru_{1-x}M_x$ (M = Co, Fe, Ni) NPs demonstrate improved OER performance compared to pure Ru, due to the incorporation of electron-rich 3d metals that modulate the electronic structure. Among these NPS, $Ru_{0.7}Co_{0.3}$ exhibits the highest activity.[157] However, a major limitation in AEM-based catalysis is the linear scaling relationship between the adsorption energies of OER intermediates, which restricts the simultaneous optimization of all reaction steps.[158] To overcome this challenge, HEA NPs have been studied as a promising class of OER catalysts.[159] Their diverse atomic environments allow different reaction intermediates to adopt distinct adsorption configurations, effectively breaking the scaling relationship. For instance, HEA CoFeNiGaZn NPs exhibit superior OER activity compared to bimetallic and ternary analogues. The combined ligand and strain effects shift the d-band center, while the adsorption free energy difference ($\Delta G_O - \Delta G_{OH}$) at the Ga sites closely aligns with the apex of the OER activity volcano plot, indicating optimized energetics.[160]

Despite their high activity, MMNP-based OER catalysts encounter ongoing durability issues due to metal dissolution in severe oxidative environments. This instability is often linked to the LOM pathway, where lattice oxygen is involved in the reaction. Although LOM can boost activity, it may also lead to catalyst degradation due to lattice oxygen loss. Reducing lattice oxygen participation by weakening the binding of oxygen species can slow oxygen diffusion and improve catalyst stability.[161] A recent study demonstrates that Ru-diluted PtCu alloys achieve both low overpotential (220 mV at 10 mA cm^{-2}) and remarkable stability. In this system, weaker oxygen binding on the PtCu surface prevents overoxidation of isolated Ru atoms, thereby reducing dissolution and promoting the AEM pathway.[162]

Overall, MMNPs provide significant benefits for OER catalysis, such as adjustable electronic structures, high intrinsic conductivity, and multifunctional active sites. However, their surfaces frequently experience oxidation or hydroxylation under OER conditions, resulting in oxide/hydroxide layers that may act as the true catalytic species.[163,164] Therefore, the future design of robust OER catalysts should integrate these structural transformations into both experimental evaluations and theoretical models to more accurately represent the dynamic nature of electrocatalyst surfaces during operation.

6. MMNPs for thermal catalysis under green chemistry conditions

Green chemistry focuses on creating sustainable solutions to environmental issues by designing chemical products and processes that reduce the use and generation of hazardous substances. Catalysis plays a crucial role in this process. It involves reducing energy consumption, minimizing chemical waste, utilizing renewable resources, and developing safer, more efficient reaction pathways.[165] MMNPs are promising catalyst candidates for green chemistry applications due to their high and adjustable activity, solid-state nature, and ease of separation from reaction media. Their multi-component composition enables precise tuning of catalytic efficiency and facilitates tandem reactions with high selectivity.

The dehydrogenation of hydrogen-rich small molecules has been extensively studied for the release of H_2 under green chemistry conditions. Two notable molecules in these studies are formic acid (HCOOH, FA)[166] and ammonia borane (NH_3BH_3, AB).[167] FA has a hydrogen content of 4.38 wt% and can be easily obtained from biomass-derived syngas synthesis[168] or directly from CO_2 reduction reactions.[169] Au, Pd, and Pt NPs show catalytic activity in FA dehydrogenation to produce H_2 and CO_2. However, their efficiency is often limited by low hydrogen production rates and poor selectivity due to the competing dehydration pathway ($HCOOH \rightarrow CO + H_2O$). The key steps in FA dehydrogenation involve C–H bond cleavage and hydrogen (H) atom desorption for H_2 recombination. Although Pd exhibits high hydrogen dissociation activity, its strong hydrogen adsorption and susceptibility to CO poisoning hinder the reaction rate. Alloying Pd with a weaker hydrogen-binding metal, such as Ag or Au, in bimetallic NPs effectively enhances FA dehydrogenation while mitigating CO poisoning due to the weak CO-binding affinity of Ag or Au.[170,171] For example, $Ag_{42}Pd_{58}$ NPs showed significantly higher catalytic activity (TOF = 382 h^{-1}) for aqueous FA dehydrogenation at 323 K compared to Pd NPs (TOF = 8.3 h^{-1}).[172] Further engineering the NPs into a core/shell AgPd/Pd structure substantially improved its activity (TOF = 21 500 h^{-1}) under similar conditions,[173] suggesting that beyond electronic effects,[174,175] strain in the thin Pd shell also contributes significantly to the catalysis enhancement. However, the promotional effects of metal on the alloy catalysis are not that simple: Ag may function not only as an electronic modifier but also as an active site in AgPd NPs.[176] Further atomic-level mechanistic studies are needed to elucidate FA dehydrogenation pathways on MMNP surfaces and, more importantly, to develop an economically viable catalyst and process for dehydrogenation. Currently, catalyst deactivation, CO contamination from competing dehydration pathways, and the need for efficient gas–liquid separation systems complicate the scale-up process. While FA itself is relatively affordable ($0.40 to $0.70 per kg), the overall viability of the process depends on developing cost-effective, durable catalysts and integrating FA production from renewable CO_2 sources to create a sustainable and economically competitive hydrogen supply chain.

Similar alloying and structural modification strategies have also been applied to study NP catalysis for AB dehydrogenation *via* hydrolysis ($NH_3BH_3 + 2H_2O \rightarrow NH_4^+ + BO_2^- + 3H_2$) or methanolysis ($NH_3BH_3 + 4CH_3OH \rightarrow NH_4^+ + B(OCH_3)_4^- + 3H_2$). AB is another attractive hydrogen storage material with high hydrogen content (~19 wt%), low toxicity, and air stability.[177] Pd-based NPs are commonly studied as active catalysts for AB methanolysis, and alloying Pd with Cu, Ni, or Fe has been shown to accelerate hydrogen production rates.[178,179] Alloying

likely modifies BH_3NH_3 adsorption properties, facilitating B–N bond cleavage, a critical step in AB dehydrogenation.[180] Recently, non-noble alloy NP catalysis for AB dehydrogenation has gained much attention.[181] Recent focus has been on Ni-based alloy NPs, such as CuNi NPs.[182,183] Despite this progress, this process is hardly commercially viable, primarily due to the high cost of AB ($50 to $300 per kg). Consequently, this reaction is more suitable for niche applications requiring high gravimetric energy density and compact hydrogen release systems, especially for direct hydrogenation reactions.

Hydrogen generated *in situ via* dehydrogenation can be directly used in tandem hydrogenation reactions catalyzed by MMNPs. This approach is both safe and environmentally friendly as it avoids the need for hydrogen separation and high-pressure conditions. Tandem hydrogenation is more generally applied in biomass conversion, pollutant remediation, and the synthesis of value-added chemicals.[184–186] For example, CuNi NPs can catalyze not only AB methanolysis but also hydrogenation of nitro and nitrile compounds (R-NO_2/R-CN) into primary amines (R-NH_2/RCH_2NH_2) with nearly quantitative yield.[182] CoNi NPs are also active for catalyzing this tandem reaction.[187] However, using AB for hydrogenation reactions does have its limitations – the other reaction products NH_3 and borates may interfere with subsequent hydrogenation steps if not removed. On the other hand, the presence of NH_3 can be further utilized as a N-source for C–N bond formation, as demonstrated in AgPd NP catalyzed AB hydrogenation of *o*-nitroacetophenone, which not only hydrogenates the nitro group, but also promotes nitrogenation of the acetyl group, forming quinazoline.[188] MMNPs have also been found to be active for catalyzing the tandem semihydrogenation of phenylacetylene to styrene[189] and the hydrodehalogenation of halogenated aromatics.[186]

Compared to AB, FA is a better agent for the hydrogenation reaction, as its dehydrogenation yields only gaseous products (CO_2 and H_2) without any liquid/solid residue accumulation in the reaction mixture. AgPd NPs can efficiently catalyze FA dehydrogenation and subsequent hydrogenation of nitroarenes with near-quantitative yields under mild conditions (1 atm, 60–80 °C).[186,190] These NPs further promote condensation of hydrogenated products with aldehydes, forming heterocycles such as benzoxazoles and quinazolines.

Tandem green chemistry strategies have also been extended to polymer synthesis. A notable example is the synthesis of poly(benzoxazole) (PBO) *via* sequential hydrogenation and condensation using AuPd NPs as a catalyst (Fig. 8(a) and (b)).[191,192] PBO is a rigid and thermally stable polymer, and has found potential applications in ballistic fibers and thermomechanical components.[193] Conventional PBO synthesis relies on polyphosphoric acid, a highly corrosive medium, and the main source of polymer contamination that is detrimental to PBO's hydrolytic stability.[194] This limitation can be addressed by using AuPd alloy NPs to catalyze the FA dehydrogenation, selective hydrogenation of 1,5-diisopropoxy-2,4-dinitrobenzene, and Schiff-base condensation with terephthalaldehyde (Fig. 8(c)), yielding PBO precursor that can be further converted to PBO *via* annealing (Fig. 8(d)). The resulting PBO shows much enhanced hydrolytic and thermal stability compared to commercial PBO (Zylon).[192] Core/shell B_2-CuPd/Pd NPs (Fig. 8(e) and (f)) are also found to be efficient for catalyzing the tandem reactions. More importantly, they show the desired selective hydrogenation of $-NO_2$ over –CHO (Fig. 8(g)), making it possible to synthesize PBO in a one-pot reaction.[195]

The examples above demonstrate that the modular catalytic properties of MMNPs enable complex chemical reactions to

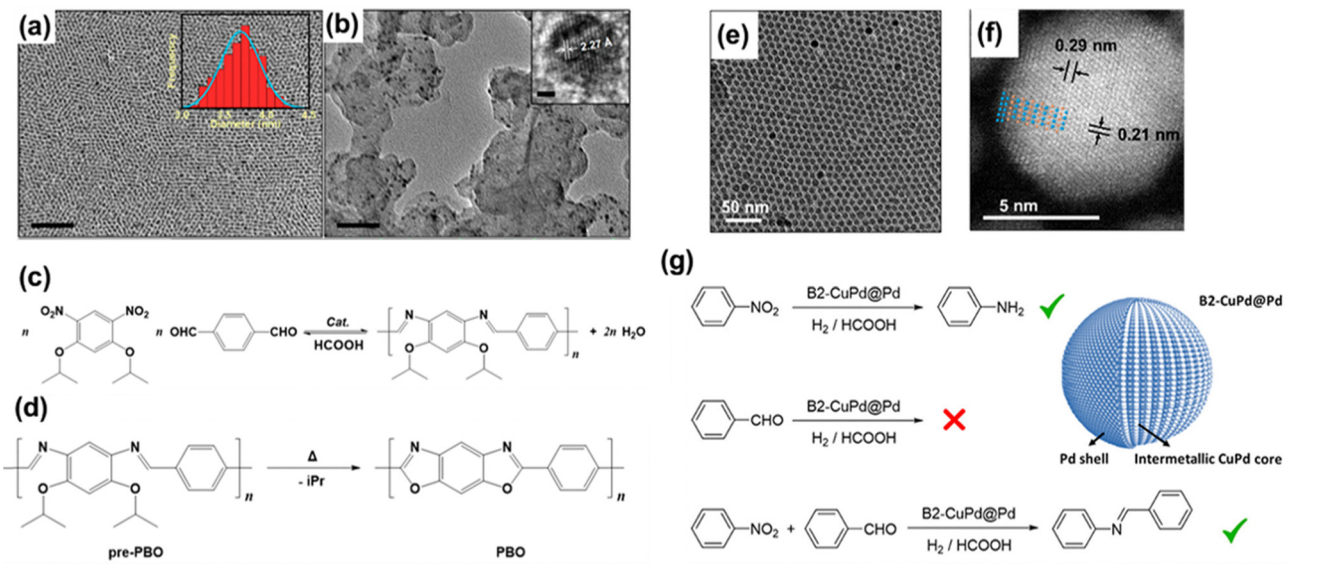

Fig. 8 (a) TEM image of AuPd NPs and (b) AuPd/C. Scale bar: 2 nm, inset 1 nm (c) One-pot synthesis of PBO precursor using diisopropoxy-2,4-dinitrobenzene and terephthalaldehyde. HCOOH is used as a hydrogen source. (d) Transformation of PBO precursor to PBO upon annealing. Reproduced from ref. 192 with permission from American Chemical Society, copyright 2021. (e) TEM images of B2-CuPd NPs with a thin Pd shell. (f) HAADF-STEM image of B2-CuPd. (g) Summary of activity of B2-CuPd with thin Pd shell in catalyzing hydrogenation of nitrobenzene, benzaldehyde, and the Schiff base condensation process. Reproduced from ref. 195 with permission from American Chemical Society, copyright 2024.

occur in a single pot, highlighting their transformative potential in green chemistry.

7. Conclusions

This review summarizes the advances in MMNPs research, including NP synthesis and applications in representative electrocatalysis and thermocatalysis. Binary and tertiary MMNPs are used as examples to illustrate synthetic and catalytic concepts before extending to multicomponent high-entropy alloys. The MMNPs discussed are categorized into three primary structural types: solid solutions, intermetallics, and heterostructures. Solid solution alloys have different metal atoms randomly distributed in the crystal structure. They provide broad compositional tunability and flexible electronic structures, allowing for property tailoring to specific catalytic reactions. Intermetallic structure features metal atoms arranged in a chemically ordered fashion with well-defined stoichiometry, which contributes to their excellent structural robustness and catalytic site uniformity. These characteristics make them highly effective in specific catalytic applications where uniformity and stability are crucial. Heterostructured MMNPs capitalize on synergistic effects at different NP interfaces, facilitating unique interactions between different materials, leading to improved performance that surpasses the capabilities of individual components.

Three structural features of MMNPs provide clear guidance for future catalyst design. For systems requiring fine-tuned activity under mild reaction conditions, solid solution NPs should be selected as catalysts. Their broad compositional tunability and flexible electronic structures allow for precise optimization of catalytic activity and selectivity. However, their chemical instability must be managed to ensure long-term durability. For applications demanding structural robustness, intermetallic NPs are the preferred choice. Their chemically ordered atomic arrangements and well-defined stoichiometry contribute to excellent structural stability and uniform catalytic sites. This makes them highly effective in environments where durability and consistency are critical, despite their limited compositional flexibility and more demanding synthesis requirements. For processes requiring multifunctional or interfacial catalysis, heterostructured NPs are the best candidates. These NPs leverage synergistic effects at interfaces, combining high activity with enhanced durability, leading to superior catalytic performance, although precise interface engineering and a deeper mechanistic understanding are necessary to fully exploit their potential. These structure–property correlations offer a comprehensive framework for rational MMNPs design tailored to specific catalytic reactions. By understanding and leveraging the distinct advantages and limitations of each structural type, one can develop more effective and specialized catalysts for a wide range of applications.

Despite the promise of MMNPs, the inherent complexity of multi-component systems makes precise design and mechanistic understanding challenging. The role of individual elements in promoting activity or stability is not yet fully understood, especially in high-entropy systems. Synthetic control over phase purity, elemental distribution, and surface termination also remains a significant hurdle. Machine/deep learning and first-principles modeling should be more broadly applied to accelerate theoretical screening of complex MMNPs and predict optimal compositions and structures. It is also important to develop high-throughput and automated synthesis/testing platforms to experimentally validate theoretical predictions and construct comprehensive structure–activity databases of MMNPs. Advanced *in situ*/operando characterization techniques should be widely adopted to track structural and electronic evolution during reactions to establish direct links between structure and function. By integrating computational design, advanced characterization, and synthetic innovation, the field is well-positioned to unlock next-generation materials for sustainable electrochemical and chemical technologies.

Beyond the conventional MMNPs summarized in this review, new concepts such as single-atom alloys,[196] intermetallic single-atom alloys,[197] and HEI structures[82,83] have recently been pursued. These architectures retain the benefits of traditional MMNPs while introducing high densities of isolated active sites or enhanced entropy-driven stability. For example, intermetallic single-atom alloys integrate isolated active atoms within robust intermetallic matrices, achieving high performance and loading, which is a challenge in traditional single-atom systems.[198] However, these novel materials require clearer structural definitions and controlled synthesis strategies to fully unlock their catalytic potential.

In all, MMNPs have emerged as a versatile and powerful platform for catalysis, offering unparalleled compositional flexibility and adjustable surface properties. This flexibility allows for the precise tuning of catalytic activity and stability, making MMNPs highly adaptable to various catalytic processes. By manipulating the electronic structure, atomic arrangement, and surface coordination environments, researchers can achieve specific catalytic behaviors tailored to desired reactions. This precise control presents a unique opportunity to delve into and exploit nanoscale structure–property relationships, providing deeper insights into how these properties influence catalytic performance. Understanding these relationships can lead to the development of more efficient and effective catalysts, paving the way for advancements in various industrial applications. However, the complexity of these manipulations requires sophisticated techniques and a thorough understanding of the underlying principles, highlighting the need for continued research and innovation in the field.

Conflicts of interest

There are no conflicts to declare.

Data availability

No primary research results, software or code have been included and no new data were generated or analyzed as part of this review.

Acknowledgements

This work was supported in part by the NSF under grants of CHE-2102290, CBET-2324345, and by Toyota.

Notes and references

1 N. Toshima and T. Yonezawa, *New J. Chem.*, 1998, **22**, 1179–1201.
2 S. Akbayrak, S. Özkar, H. Kim, T. Y. Yoo, M. S. Bootharaju, J. H. Kim, D. Y. Chung and T. Hyeon, *Adv. Sci.*, 2022, **9**, 2104054.
3 B. A. Yusuf, W. Yaseen, J. Xie, A. A. Babangida, A. I. Muhammad, M. Xie and Y. Xu, *Nano Energy*, 2022, **104**, 107959.
4 Z. Cui, W. Jiao, Z. Huang, G. Chen, B. Zhang, Y. Han and W. Huang, *Small*, 2023, **19**, 2301465.
5 D. J. Loevlie, B. Ferreira and G. Mpourmpakis, *Acc. Chem. Res.*, 2023, **56**, 248–257.
6 H. Duan, D. Wang and Y. Li, *Chem. Soc. Rev.*, 2015, **44**, 5778–5792.
7 S. Sun, S. Anders, T. Thomson, J. E. E. Baglin, M. F. Toney, H. F. Hamann, C. B. Murray and B. D. Terris, *J. Phys. Chem. B*, 2003, **11**, 5419–5425.
8 M. Nakaya, Y. Tsuchiya, K. Ito, Y. Oumi, T. Sano and T. Teranishi, *Chem. Lett.*, 2004, **33**, 130–131.
9 V. Mazumder, M. Chi, M. N. Mankin, Y. Liu, Ö. Metin, D. Sun, K. L. More and S. Sun, *Nano Lett.*, 2012, **12**, 1102–1106.
10 S. Sun, C. B. Murray, D. Weller, L. Folks and A. Moser, *Science*, 2000, **287**, 1989–1992.
11 V. F. Puntes, K. M. Krishnan and A. P. Alivisatos, *Science*, 2001, **291**, 2115–2117.
12 S. Sun and H. Zeng, *J. Am. Chem. Soc.*, 2002, **124**, 8204–8205.
13 R.-Y. Shao, X.-C. Xu, Z.-H. Zhou, W.-J. Zeng, T.-W. Song, P. Yin, A. Li, C.-S. Ma, L. Tong, Y. Kong and H.-W. Liang, *Nat. Commun.*, 2023, **14**, 5896.
14 G. Chen, S. Desinan, R. Rosei, F. Rosei and D. Ma, *Chem. – Eur. J.*, 2012, **18**, 7925–7930.
15 K. Kusada, H. Kobayashi, R. Ikeda, Y. Kubota, M. Takata, S. Toh, T. Yamamoto, S. Matsumura, N. Sumi, K. Sato, K. Nagaoka and H. Kitagawa, *J. Am. Chem. Soc.*, 2014, **18**, 1864–1871.
16 B. Huang, H. Kobayashi, T. Yamamoto, S. Matsumura, Y. Nishida, K. Sato, K. Nagaoka, S. Kawaguchi, Y. Kubota and H. Kitagawa, *J. Am. Chem. Soc.*, 2017, **139**, 4643–4646.
17 T. Komatsu, H. Kobayashi, K. Kusada, Y. Kubota, M. Takata, T. Yamamoto, S. Matsumura, K. Sato, K. Nagaoka and H. Kitagawa, *Chem. – Eur. J.*, 2017, **23**, 57–60.
18 S. Guo and S. Sun, *J. Am. Chem. Soc.*, 2012, **134**, 2492–2495.
19 J. Li, S. Sharma, X. Liu, Y.-T. Pan, J. S. Spendelow, M. Chi, Y. Jia, P. Zhang, D. A. Cullen, Z. Xi, H. Lin, Z. Yin, B. Shen, M. Muzzio, C. Yu, Y. S. Kim, A. A. Peterson, K. L. More, H. Zhu and S. Sun, *Joule*, 2019, **3**, 124–135.
20 J. Li, S. Sharma, K. Wei, Z. Chen, D. Morris, H. Lin, C. Zeng, M. Chi, Z. Yin, M. Muzzio, M. Shen, P. Zhang, A. A. Peterson and S. Sun, *J. Am. Chem. Soc.*, 2020, **142**, 19209–19216.
21 J. Li and S. Sun, *Acc. Chem. Res.*, 2019, **52**, 2015–2025.
22 J. Guan, D. Dong, N. A. Khan and Y. Zheng, *Chem. Commun.*, 2024, **60**, 1811–1825.
23 Y. Yan, J. S. Du, K. D. Gilroy, D. Yang, Y. Xia and H. Zhang, *Adv. Mater.*, 2017, **29**, 1605997.
24 J. Kim, Y. Lee and S. Sun, *J. Am. Chem. Soc.*, 2010, **132**, 4996–4997.
25 D. Zhang, B. Gökce and S. Barcikowski, *Adv. Funct. Mater.*, 2023, **13**, 10988–11000.
26 B. M. Leonard, Q. Zhou, D. Wu and F. J. DiSalvo, *Chem. Mater.*, 2011, **23**, 1136–1146.
27 A. C. Foucher, S. Yang, D. J. Rosen, R. Huang, J. B. Pyo, O. Kwon, C. J. Owen, D. F. Sanchez, I. I. Sadykov, D. Grolimund, B. Kozinsky, A. I. Frenkel, R. J. Gorte, C. B. Murray and E. A. Stach, *J. Am. Chem. Soc.*, 2023, **145**, 5410–5421.
28 Z. Qi, C. Xiao, C. Liu, T. W. Goh, L. Zhou, R. Maligal-Ganesh, Y. Pei, X. Li, L. A. Curtiss and W. Huang, *J. Am. Chem. Soc.*, 2021, **4**, 1179–1201.
29 H. Lv, Y. Zheng, Y. Wang, J. Wang, B. Liu and Z.-A. Qiao, *Angew. Chem., Int. Ed.*, 2023, **62**, e202304420.
30 H.-S. Chen, T. M. Benedetti, V. R. Gonçales, N. M. Bedford, R. W. J. Scott, R. F. Webster, S. Cheong, J. J. Gooding and R. D. Tilley, *J. Am. Chem. Soc.*, 2020, **142**, 3231–3239.
31 X. Ji, K. T. Lee, R. Holden, L. Zhang, J. Zhang, G. A. Botton, M. Couillard and L. F. Nazar, *Nat. Chem.*, 2010, **2**, 286–293.
32 J. Li, Z. Xi, Y.-T. Pan, J. S. Spendelow, P. N. Duchesne, D. Su, Q. Li, C. Yu, Z. Yin, B. Shen, Y. S. Kim, P. Zhang and S. Sun, *J. Am. Chem. Soc.*, 2018, **140**, 2926–2932.
33 H. Chen, D. Wang, Y. Yu, K. A. Newton, D. A. Muller, H. Abruña and F. J. DiSalvo, *J. Am. Chem. Soc.*, 2012, **134**, 18453–18459.
34 D. Y. Chung, S. W. Jun, G. Yoon, S. G. Kwon, D. Y. Shin, P. Seo, J. M. Yoo, H. Shin, Y.-H. Chung, H. Kim, B. S. Mun, K.-S. Lee, N.-S. Lee, S. J. Yoo, D.-H. Lim, K. Kang, Y.-E. Sung and T. Hyeon, *J. Am. Chem. Soc.*, 2015, **137**, 15478–15485.
35 T.-W. Song, C. Xu, Z.-T. Sheng, H.-K. Yan, L. Tong, J. Liu, W.-J. Zeng, L.-J. Zuo, P. Yin, M. Zuo, S.-Q. Chu, P. Chen and H.-W. Liang, *Nat. Commun.*, 2022, **13**, 6521.
36 S. Zhang, S. Guo, H. Zhu, D. Su and S. Sun, *J. Am. Chem. Soc.*, 2012, **134**, 5060–5063.
37 H. Wang, P. Shang, J. Zhang, M. Guo, Y. Mu, Q. Li and H. Wang, *Chem. Mater.*, 2013, **25**, 2450–2454.
38 J. Liang, Y. Wan, H. Lv, X. Liu, F. Lv, S. Li, J. Xu, Z. Deng, J. Liu, S. Zhang, Y. Sun, M. Luo, G. Lu, J. Han, G. Wang, Y. Huang, S. Guo and Q. Li, *Nat. Mater.*, 2024, **23**, 1259–1267.
39 W. Lei, J. Xu, Y. Yu, W. Yang, Y. Hou and D. Chen, *Nano Lett.*, 2018, **18**, 7839–7844.
40 K. Jiang, P. Wang, S. Guo, X. Zhang, X. Shen, G. Lu, D. Su, X. Huang, C. Wang, D. P. Chen, X. Sang, R. R. Unocic and S. E. Skrabalak, *ACS Nano*, 2016, **10**, 6345–6353.
41 J. K. Mathiesen, E. D. Bøjesen, J. K. Pedersen, E. T. S. Kjær, M. Juelsholt, S. Cooper, J. Quinson, A. S. Anker, G. Cutts, D. S. Keeble, M. S. Thomsen, J. Rossmeisl and K. M. Ø. Jensen, *Small Methods*, 2022, **6**, 2200420.
42 H. Li, J. Lai, Z. Li and L. Wang, *ACS Catal.*, 2019, **2**, 1370–1380.
43 J. Qiu, Q. N. Nguyen, Z. Lyu, Q. Wang and Y. Xia, *Adv. Mater.*, 2021, **34**, 2102591.
44 Y. Song, K. Liu and S. Chen, *Langmuir*, 2012, **28**, 17143–17152.
45 B. Ni, P. He, W. Liao, S. Chen, L. Gu, Y. Gong, K. Wang, J. Zhuang, L. Song, G. Zhou and X. Wang, *Small*, 2018, **14**, 1703749.
46 C. Wang, Y. Shi, D. Qin, Y. Xia, Y. Song, K. Liu and S. Chen, *Nanoscale Horiz.*, 2023, **8**, 1194–1204.
47 M. Zhou, H. Wang, A. O. Elnabawy, Z. D. Hood, M. Chi, P. Xiao, Y. Zhang, M. Mavrikakis and Y. Xia, *Chem. Mater.*, 2019, **31**, 1370–1380.
48 X. Sun, D. Li, S. Guo, W. Zhu and S. Sun, *Nanoscale*, 2016, **8**, 2626–2631.
49 P. Strasser, S. Koh, T. Anniyev, J. Greeley, K. More, C. Yu, Z. Liu, S. Kaya, D. Nordlund, H. Ogasawara, M. F. Toney and A. Nilsson, *Nat. Chem.*, 2010, **2**, 454–460.
50 M. Zhao, Z. Chen, Z. Lyu, Z. D. Hood, M. Xie, M. Vara, M. Chi and Y. Xia, *J. Am. Chem. Soc.*, 2019, **141**, 7028–7036.
51 S.-I. Choi, A. Young, S. R. Lee, C. Ma, M. Luo, M. Chi, C.-K. Tsung and Y. Xia, *Nanoscale Horiz.*, 2019, **4**, 1232–1238.
52 Y. Ma, M. Sun, H. Xu, Q. Zhang, J. Lv, W. Guo, F. Hao, W. Cui, Y. Wang, J. Yin, H. Wen, P. Lu, G. Wang, J. Zhou, J. Yu, C. Ye, L. Gan, D. Zhang, S. Chu, L. Gu, M. Shao, B. Huang and Z. Fan, *Adv. Mater.*, 2024, **36**, 2402979.
53 X. Zhou, Y. Ma, Y. Ge, S. Zhu, Y. Cui, B. Chen, L. Liao, Q. Yun, Z. He, H. Long, L. Li, B. Huang, Q. Luo, L. Zhai, X. Wang, L. Bai, G. Wang, Z. Guan, Y. Chen, C.-S. Lee, J. Wang, C. Ling, M. Shao, Z. Fan and H. Zhang, *J. Am. Chem. Soc.*, 2021, **144**, 547–555.
54 F.-R. Fan, D.-Y. Liu, Y.-F. Wu, S. Duan, Z.-X. Xie, Z.-Y. Jiang and Z.-Q. Tian, *J. Am. Chem. Soc.*, 2008, **8**, 6949–6951.
55 V. D. Pawlik, A. Janssen, Y. Ding and Y. Xia, *J. Phys. Chem. C*, 2024, **128**, 1377–1385.
56 X. Lyu, Y. Jia, X. Mao, D. Li, G. Li, L. Zhuang, X. Wang, D. Yang, Q. Wang, A. Du and X. Yao, *Adv. Mater.*, 2020, **32**, 2003493.
57 M. Vara, L. T. Roling, X. Wang, A. O. Elnabawy, Z. D. Hood, M. Chi, M. Mavrikakis and Y. Xia, *ACS Nano*, 2017, **11**, 4571–4581.
58 K. D. Gilroy, A. Ruditskiy, H.-C. Peng, D. Qin and Y. Xia, *Chem. Rev.*, 2016, **116**, 10414–10472.
59 S. Liu, S. Guo, S. Sun and X.-Z. You, *Nanoscale*, 2015, **7**, 4890–4893.
60 W. Yang, W. Lei, Y. Yu, W. Zhu, T. A. George, X.-Z. Li, D. J. Sellmyer and S. Sun, *J. Mater. Chem. C*, 2015, **3**, 7075–7080.
61 M. N. Tahir, F. Natalio, M. A. Cambaz, M. Panthöfer, R. Branscheid, U. Kolb and W. Tremel, *Nanoscale*, 2013, **5**, 9944.

62 A. Mendoza-Garcia and S. Sun, *Adv. Funct. Mater.*, 2016, **26**, 3809–3817.
63 J. Zeng, C. Zhu, J. Tao, M. Jin, H. Zhang, Z.-Y. Li, Y. Zhu and Y. Xia, *Angew. Chem., Int. Ed.*, 2012, **51**, 2354–2358.
64 X. Qiu, V. Pawlik, S. Zhou, J. Tao and Y. Xia, *J. Am. Chem. Soc.*, 2023, **145**, 13400–13410.
65 Y. Feng, Y. Wang, J. He, X. Song, Y. Y. Tay, H. H. Hng, X. Y. Ling and H. Chen, *J. Am. Chem. Soc.*, 2015, **137**, 7624–7627.
66 J. Feng, F. Yang, X. Wang, F. Lyu, Z. Li and Y. Yin, *Adv. Mater.*, 2019, **31**, 1900789.
67 B. Liu, S. Thanneeru, A. Lopes, L. Jin, M. McCabe and J. He, *Small*, 2017, **13**, 1700091.
68 H. Duan, H. Tan and J. He, *Nano Res.*, 2025, **18**, 94907147.
69 Q. Wang, Z. L. Zhao and M. Gu, *Small*, 2019, **15**, 1903122.
70 Y. Y. Chen, T. Duval, U. D. Hung, J. W. Yeh, H. C. Shih, J. Li, S. Sharma, K. Wei, Z. Chen, D. Morris, H. Lin, C. Zeng, M. Chi, Z. Yin, M. Muzzio, M. Shen, P. Zhang, A. A. Peterson, S. Sun, T. A. A. Batchelor, J. K. Pedersen, S. H. Winther, I. E. Castelli, K. W. Jacobsen and J. Rossmeisl, *Joule*, 2005, **47**, 2257–2279.
71 Y. Yao, Z. Huang, P. Xie, S. D. Lacey, R. J. Jacob, H. Xie, F. Chen, A. Nie, T. Pu and M. Rehwoldt, *Science*, 2018, **359**, 1489–1494.
72 W. Ji, W. Wang, H. Wang, J. Zhang, Y. Wang, F. Zhang and Z. Fu, *Intermetallics*, 2015, **56**, 24–27.
73 H. Lin, M. Muzzio, K. Wei, P. Zhang, J. Li, N. Li, Z. Yin, D. Su and S. Sun, *Angew. Chem., Int. Ed.*, 2019, **9**, 18547–18558.
74 J. Johny, Y. Li, M. Kamp, O. Prymak, S.-X. Liang, T. Krekeler, M. Ritter, L. Kienle, C. Rehbock, S. Barcikowski and S. Reichenberger, *Nano Res.*, 2022, **15**, 4807–4819.
75 D. Wu, K. Kusada, T. Yamamoto, T. Toriyama, S. Matsumura, I. Gueye, O. Seo, J. Kim, S. Hiroi, O. Sakata, S. Kawaguchi, Y. Kubota and H. Kitagawa, *Chem. Sci.*, 2020, **11**, 12731–12736.
76 Y. Chen, X. Zhan, S. L. A. Bueno, I. H. Shafei, H. M. Ashberry, K. Chatterjee, L. Xu, Y. Tang and S. E. Skrabalak, *Nanoscale Horiz.*, 2021, **6**, 231–237.
77 C. Moreira Da Silva, H. Amara, F. Fossard, A. Girard, A. Loiseau and V. Huc, *Nanoscale*, 2022, **14**, 9832–9841.
78 P.-C. Chen, X. Liu, J. L. Hedrick, Z. Xie, S. Wang, Q.-Y. Lin, M. C. Hersam, V. P. Dravid and C. A. Mirkin, *Science*, 2016, **352**, 1565–1569.
79 S. L. A. Bueno, A. Leonardi, N. Kar, K. Chatterjee, X. Zhan, C. Chen, Z. Wang, M. Engel, V. Fung and S. E. Skrabalak, *ACS Nano*, 2022, **16**, 18873–18885.
80 G. Cao, J. Liang, Z. Guo, K. Yang, G. Wang, H. Wang, X. Wan, Z. Li, Y. Bai, Y. Zhang, J. Liu, Y. Feng, Z. Zheng, C. Lu, G. He, Z. Xiong, Z. Liu, S. Chen, Y. Guo, M. Zeng, J. Lin and L. Fu, *Nature*, 2023, **619**, 73–77.
81 M. Cui, C. Yang, S. Hwang, M. Yang, S. Overa, Q. Dong, Y. Yao, A. H. Brozena, D. A. Cullen, M. Chi, T. F. Blum, D. Morris, Z. Finfrock, X. Wang, P. Zhang, V. G. Goncharov, X. Guo, J. Luo, Y. Mo, F. Jiao and L. Hu, *Sci. Adv.*, 2022, **8**, eabm4322.
82 G. Feng, F. Ning, Y. Pan, T. Chen, J. Song, Y. Wang, R. Zou, D. Su and D. Xia, *J. Am. Chem. Soc.*, 2023, **145**, 11140–11150.
83 D. Wang, Z. Chen, Y. Wu, Y. Huang, L. Tao, J. Chen, C. Dong, C. V. Singh and S. Wang, *Sci. China Mater.*, 2021, **64**, 2454–2466.
84 Z. Ma, J. Mohapatra, K. Wei, J. P. Liu and S. Sun, *Chem. Rev.*, 2023, **123**, 3904–3943.
85 M. Che, *Catal. Today*, 2013, **218–219**, 162–171.
86 H. Lin, Y. Liu, J. Deng, L. Jing, Z. Wang, L. Wei, Z. Wei, Z. Hou, J. Tao and H. Dai, *Environ. Sci. Adv.*, 2025, **4**, 33–56.
87 S. Bhattacharjee, U. V. Waghmare and S.-C. Lee, *Sci. Rep.*, 2016, **6**, 35916.
88 L. Sun, K. Wen, G. Li, X. Zhang, X. Zeng, B. Johannessen and S. Zhang, *ACS Mater. Au*, 2024, **4**, 547–556.
89 N. Hashimoto, K. Mori, H. Yoshida, N. Kamiuchi, R. Kitaura, R. Hirasawa and H. Yamashita, *Nano Lett.*, 2024, **24**, 7063–7068.
90 A. Mehta and Y. Sohn, *Mater. Res. Lett.*, 2021, **9**, 239–246.
91 E. Lotfi-Khojasteh, H. Elmkhah, M. Nouri and P. H. Mayrhofer, *Adv. Eng. Mater.*, 2024, **26**, 2301934.
92 H. Kuang, Z. Xu, X. Tan, K. Yu and C. Chen, *Small*, 2024, **20**, 2308421.
93 J. Hao, F. Ma, Y. Chen, S. Lu, F. Duan, M. Du, C. Wang, W. Zhang and H. Zhu, *New J. Chem.*, 2024, **48**, 511–514.
94 T. Chen, C. Qiu, X. Zhang, H. Wang, J. Song, K. Zhang, T. Yang, Y. Zuo, Y. Yang, C. Gao, W. Xiao, Z. Jiang, Y. Wang, Y. Xiang and D. Xia, *J. Am. Chem. Soc.*, 2023, **146**, 1174–1184.
95 J. Rosen, G. S. Hutchings, Q. Lu, S. Rivera, Y. Zhou, D. G. Vlachos and F. Jiao, *ACS Catal.*, 2015, **5**, 4293–4299.
96 W. Zhu, R. Michalsky, Ö. Metin, H. Lv, S. Guo, C. J. Wright, X. Sun, A. A. Peterson and S. Sun, *J. Am. Chem. Soc.*, 2013, **135**, 16833–16836.
97 S. Liu, H. Tao, L. Zeng, Q. Liu, Z. Xu, Q. Liu and J.-L. Luo, *J. Am. Chem. Soc.*, 2017, **139**, 2160–2163.
98 D. Gao, H. Zhou, F. Cai, J. Wang, G. Wang and X. Bao, *ACS Catal.*, 2018, **8**, 1510–1519.
99 X. Yuan, L. Zhang, L. Li, H. Dong, S. Chen, W. Zhu, C. Hu, W. Deng, Z.-J. Zhao and J. Gong, *J. Am. Chem. Soc.*, 2019, **141**, 4791–4794.
100 R. Lin, X. Ma, W.-C. Cheong, C. Zhang, W. Zhu, J. Pei, K. Zhang, B. Wang, S. Liang, Y. Liu, Z. Zhuang, R. Yu, H. Xiao, J. Li, D. Wang, Q. Peng, C. Chen and Y. Li, *Nano Res.*, 2019, **12**, 2866–2871.
101 Y. Mun, S. Lee, A. Cho, S. Kim, J. W. Han and J. Lee, *Appl. Catal., B*, 2019, **246**, 82–88.
102 S. Wei, Y. Xu, T. Song, H. Dai, F. Li, X. Gao, Y. Zhai, S. Gong, R. Li, X. Zhang and K. Chan, *J. Am. Chem. Soc.*, 2025, **147**, 4219–4229.
103 D. Kim, J. Resasco, Y. Yu, A. M. Asiri and P. Yang, *Nat. Commun.*, 2014, **5**, 4948.
104 D. Kim, C. Xie, N. Becknell, Y. Yu, M. Karamad, K. Chan, E. J. Crumlin, J. K. Nørskov and P. Yang, *J. Am. Chem. Soc.*, 2017, **139**, 8329–8336.
105 S. Kuang, M. Li, X. Chen, H. Chi, J. Lin, Z. Hu, S. Hu, S. Zhang and X. Ma, *Chin. Chem. Lett.*, 2023, **34**, 108013.
106 S. Liu, H. Tao, L. Zeng, Q. Liu, Z. Xu, Q. Liu, J.-L. Luo, A. N. Kuhn, H. Zhao, U. O. Nwabara, X. Lu, M. Liu, Y. Pan, W. Zhu, P. J. A. Kenis and H. Yang, *Adv. Funct. Mater.*, 2021, **31**, 2101668.
107 V. Okatenko, A. Loiudice, M. A. Newton, D. C. Stoian, A. Blokhina, A. N. Chen, K. Rossi and R. Buonsanti, *Adv. Funct. Mater.*, 2021, **31**, 2101668.
108 Y. Zhao, Y. Wang, Z. Yu, C. Song, J. Wang, H. Huang, L. Meng, M. Liu and L. Liu, *ACS Nano*, 2025, **19**, 4505–4514.
109 S. Jeong, C. Huang, Z. Levell, R. X. Skalla, W. Hong, N. J. Escorcia, Y. Losovyj, B. Zhu, A. N. Butrum-Griffith, Y. Liu, C. W. Li, D. Reifsnyder Hickey, Y. Liu and X. Ye, *J. Am. Chem. Soc.*, 2024, **146**, 4508–4520.
110 L. Xiong, X. Zhang, H. Yuan, J. Wang, X. Yuan, Y. Lian, H. Jin, H. Sun, Z. Deng, D. Wang, J. Hu, H. Hu, J. Choi, J. Li, Y. Chen, J. Zhong, J. Guo, M. H. Rümmerli, L. Xu, Y. Peng, S. Ma, M. Sadakiyo, M. Heima, R. Luo, R. T. Haasch, J. I. Gold, M. Yamauchi, P. J. A. Kenis, V. Okatenko, A. Loiudice, M. A. Newton, D. C. Stoian, A. Blokhina, A. N. Chen, K. Rossi, R. Buonsanti, A. N. Kuhn, H. Zhao, U. O. Nwabara, X. Lu, M. Liu, Y. Pan, W. Zhu, P. J. A. Kenis and H. Yang, *Adv. Funct. Mater.*, 2021, **60**, 2508–2518.
111 Y. Chen, Z. Fan, J. Wang, C. Ling, W. Niu, Z. Huang, G. Liu, B. Chen, Z. Lai, X. Liu, B. Li, Y. Zong, L. Gu, J. Wang, X. Wang and H. Zhang, *J. Am. Chem. Soc.*, 2020, **142**, 12760–12766.
112 S. Ma, M. Sadakiyo, M. Heima, R. Luo, R. T. Haasch, J. I. Gold, M. Yamauchi and P. J. A. Kenis, *J. Am. Chem. Soc.*, 2017, **139**, 47–50.
113 S. Zhang, B. Zhang, S. Yang, T. Shao, X. Li, R. Cao and M. Cao, *ACS Appl. Nano Mater.*, 2025, **8**, 1893–1902.
114 J. Huang, M. Mensi, E. Oveisi, V. Mantella and R. Buonsanti, *J. Am. Chem. Soc.*, 2019, **141**, 2490–2499.
115 H. Li, J. Lai, Z. Li and L. Wang, *Adv. Funct. Mater.*, 2021, **109**, 2106715.
116 H. Li, X. Li, P. Wang, Z. Zhang, K. Davey, J. Q. Shi and S.-Z. Qiao, *J. Am. Chem. Soc.*, 2024, **146**, 22850–22858.
117 Z. W. Chen, Z. Gariepy, L. Chen, X. Yao, A. Anand, S.-J. Liu, C. G. Tetsassi Feugmo, I. Tamblyn and C. V. Singh, *ACS Catal.*, 2022, **12**, 14864–14871.
118 H. Li, H. Huang, Y. Chen, F. Lai, H. Fu, L. Zhang, N. Zhang, S. Bai and T. Liu, *Adv. Mater.*, 2023, **35**, 2209242.
119 P.-C. Chen, C. Chen, Y. Yang, A. L. Maulana, J. Jin, J. Feijoo and P. Yang, *J. Am. Chem. Soc.*, 2023, **145**, 10116–10125.
120 V. Okatenko, A. Loiudice, M. A. Newton, D. C. Stoian, A. Blokhina, A. N. Chen, K. Rossi and R. Buonsanti, *J. Am. Chem. Soc.*, 2023, **145**, 5370–5383.
121 V. Tripković, E. Skúlason, S. Siahrostami, J. K. Nørskov and J. Rossmeisl, *Electrochim. Acta*, 2010, **55**, 7975–7981.
122 J. Zhao, J. Lian, Z. Zhao, X. Wang and J. Zhang, *Nano-Micro Lett.*, 2023, **15**, 19.
123 Z. Zhao, C. Chen, Z. Liu, J. Huang, M. Wu, H. Liu, Y. Li and Y. Huang, *Adv. Mater.*, 2019, **31**, 1808115.

124 T. Wang, J. Liang, Z. Zhao, S. Li, G. Lu, Z. Xia, C. Wang, J. Luo, J. Han, C. Ma, Y. Huang and Q. Li, *Adv. Energy Mater.*, 2019, **9**, 1803771.
125 J. Greeley, I. E. L. Stephens, A. S. Bondarenko, T. P. Johansson, H. A. Hansen, T. F. Jaramillo, J. Rossmeisl, I. Chorkendorff and J. K. Nørskov, *Nat. Chem.*, 2009, **1**, 552–556.
126 M. Escudero-Escribano, P. Malacrida, M. H. Hansen, U. G. Vej-Hansen, A. Velazquez-Palenzuela, V. Tripkovic, J. Schiotz, J. Rossmeisl, I. E. L. Stephens and I. Chorkendorff, *Science*, 2016, **352**, 73–76.
127 J. Liang, Z. Zhao, N. Li, X. Wang, S. Li, X. Liu, T. Wang, G. Lu, D. Wang and B.-J. Hwang, *Adv. Energy Mater.*, 2020, **10**, 2000179.
128 W. Niu, S. Pakhira, G. Cheng, F. Zhao, N. Yao, J. L. Mendoza-Cortes and B. E. Koel, *Nat. Mater.*, 2024, **23**, 1704–1711.
129 Z. An, H. Li, X. Zhang, Z. Xia, H. Zhang, W. Chu, S. Yu, S. Wang and G. Sun, *ACS Catal.*, 2024, **14**, 2572–2581.
130 X. Liu, Y. Wang, J. Liang, S. Li, S. Zhang, D. Su, Z. Cai, Y. Huang, L. Elbaz, Q. Li, W.-W. Zhan, Q.-L. Zhu and Q. Xu, *J. Am. Chem. Soc.*, 2024, **146**, 2033–2042.
131 T. Chen, F. Ning, J. Qi, G. Feng, Y. Wang, J. Song, T. Yang, X. Liu, L. Chen and D. Xia, *iScience*, 2023, **26**, 105890.
132 L. Zhang, X. Zhang, C. Chen, J. Zhang, W. Tan, Z. Xu, Z. Zhong, L. Du, H. Song, S. Liao, Y. Zhu, Z. Zhou and Z. Cui, *Angew. Chem., Int. Ed.*, 2024, **136**, e202411123.
133 X. Fu, C. Wan, Y. Huang and X. Duan, *Science*, 2003, **125**, 3680–3681.
134 S. M. M. Ehteshami and S. H. Chan, *Electrochim. Acta*, 2013, **93**, 334–345.
135 Y. X. Chen, A. Miki, S. Ye, H. Sakai and M. Osawa, *J. Mater. Chem. A*, 2018, **6**, 8531–8536.
136 T. Frelink, W. Visscher and J. A. R. van Veen, *Surf. Sci.*, 1995, **335**, 353–360.
137 J. Creus, J. De Tovar, N. Romero, J. García-Antón, K. Philippot, R. Bofill, X. Sala, B. Jiang, Y. Guo, J. Kim, A. E. Whitten, K. Wood, K. Kani, A. E. Rowan, J. Henzie and Y. Yamauchi, *J. Mater. Chem. A*, 2020, **8**, 2323–2330.
138 T. Holm, S. Sunde, F. Seland, D. A. Harrington, J. Li, S. Sharma, X. Liu, Y.-T. Pan, J. S. Spendelow, M. Chi, Y. Jia, P. Zhang, D. A. Cullen, Z. Xi, H. Lin, Z. Yin, B. Shen, M. Muzzio, C. Yu, Y. S. Kim, A. A. Peterson, K. L. More, H. Zhu, S. Sun, L. Hui, Y. Xue, C. Xing, Y. Liu, Y. Du, Y. Fang, H. Yu, C. Zhang, F. He and Y. Li, *Nano Energy*, 2019, **323**, 134764.
139 H. Li, Y. Han, H. Zhao, W. Qi, D. Zhang, Y. Yu, W. Cai, S. Li, J. Lai, B. Huang and L. Wang, *Nat. Commun.*, 2020, **11**, 5437.
140 R. Kavanagh, X.-M. Cao, W.-F. Lin, C. Hardacre and P. Hu, *Angew. Chem., Int. Ed.*, 2012, **51**, 1572–1575.
141 L. Wang, W. Gao, Z. Liu, Z. Zeng, Y. Liu, M. Giroux, M. Chi, G. Wang, J. Greeley, X. Pan and C. Wang, *ACS Catal.*, 2018, **8**, 35–42.
142 W. Du, K. E. Mackenzie, D. F. Milano, N. A. Deskins, D. Su and X. Teng, *ACS Catal.*, 2012, **2**, 287–297.
143 H. Lin, M. Muzzio, K. Wei, P. Zhang, J. Li, N. Li, Z. Yin, D. Su and S. Sun, *ACS Appl. Energy Mater.*, 2019, **2**, 8701–8706.
144 W. Huang, X. Kang, C. Xu, J. Zhou, J. Deng, Y. Li and S. Cheng, *Adv. Mater.*, 2017, **29**, 1703057.
145 S. Luo, L. Zhang, Y. Liao, L. Li, Q. Yang, X. Wu, X. Wu, D. He, C. He and W. Chen, *Adv. Mater.*, 2021, **33**, 2008508.
146 W. Zhang, Y. Yang, B. Huang, F. Lv, K. Wang, N. Li, M. Luo, Y. Chao, Y. Li and Y. Sun, *Adv. Mater.*, 2019, **31**, 1805833.
147 K. Wei, H. Lin, X. Zhao, Z. Zhao, N. Marinkovic, M. Morales, Z. Huang, L. Perlmutter, H. Guan, C. Harris, M. Chi, G. Lu, K. Sasaki and S. Sun, *J. Am. Chem. Soc.*, 2023, **145**, 19076–19085.
148 Z. Liang, L. Song, S. Deng, Y. Zhu, E. Stavitski, R. R. Adzic, J. Chen and J. X. Wang, *J. Am. Chem. Soc.*, 2019, **141**, 9629–9636.
149 J. Li, S. Z. Jilani, H. Lin, X. Liu, K. Wei, Y. Jia, P. Zhang, M. Chi, Y. J. Tong, Z. Xi and S. Sun, *J. Am. Chem. Soc.*, 2019, **58**, 11527–11533.
150 D. Wu, K. Kusada, T. Yamamoto, T. Toriyama, S. Matsumura, S. Kawaguchi, Y. Kubota and H. Kitagawa, *J. Am. Chem. Soc.*, 2020, **142**, 13833–13838.
151 H. Minamihara, K. Kusada, T. Yamamoto, T. Toriyama, Y. Murakami, S. Matsumura, L. S. R. Kumara, O. Sakata, S. Kawaguchi, Y. Kubota, O. Seo, S. Yasuno and H. Kitagawa, *J. Am. Chem. Soc.*, 2023, **145**, 17136–17142.
152 M. Cui, C. Yang, S. Hwang, M. Yang, S. Overa, Q. Dong, Y. Yao, A. H. Brozena, D. A. Cullen, M. Chi, T. F. Blum, D. Morris, Z. Finfrock, X. Wang, P. Zhang, V. G. Goncharov, X. Guo, J. Luo, Y. Mo, F. Jiao and L. Hu, *Electrochim. Acta*, 2022, **8**, eabm4322.
153 Q. Shi, C. Zhu, D. Du and Y. Lin, *Chem. Soc. Rev.*, 2019, **48**, 3181–3192.
154 L. Wu, Q. Li, C. H. Wu, H. Zhu, A. Mendoza-Garcia, B. Shen, J. Guo and S. Sun, *J. Am. Chem. Soc.*, 2015, **137**, 7071–7074.
155 L. Han, S. Dong and E. Wang, *Adv. Mater.*, 2016, **28**, 9266–9291.
156 M. Yu, E. Budiyanto and H. Tüysüz, *Angew. Chem., Int. Ed.*, 2022, **61**, e202103824.
157 H. Wang, Y. Yang, F. J. DiSalvo and H. D. Abruña, *ACS Catal.*, 2020, **10**, 4608–4616.
158 M. J. Craig, G. Coulter, E. Dolan, J. Soriano-López, E. Mates-Torres, W. Schmitt, M. García-Melchor, Y. Da, R. Jiang, Z. Tian, X. Han, W. Chen and W. Hu, *Nat. Commun.*, 2019, **10**, 4993.
159 T. A. A. Batchelor, J. K. Pedersen, S. H. Winther, I. E. Castelli, K. W. Jacobsen and J. Rossmeisl, *Joule*, 2019, **3**, 834–845.
160 L. Sharma, N. K. Katiyar, A. Parui, R. Das, R. Kumar, C. S. Tiwary, A. K. Singh, A. Halder and K. Biswas, *Nano Res.*, 2022, 1–8.
161 Y. Da, R. Jiang, Z. Tian, X. Han, W. Chen and W. Hu, *SmartMat*, 2023, **4**, e1136.
162 S. Li, Y. Yang, S. Huang, H. Li, J. Lai, Z. Li, L. Wang, C. Bianchini and P. K. Shen, *Science*, 2021, **2**, 304–313.
163 Y. Sun, X. Zhang, M. Luo, X. Chen, L. Wang, Y. Li, M. Li, Y. Qin, C. Li, N. Xu, G. Lu, P. Gao and S. Guo, *Adv. Mater.*, 2018, **30**, 1802136.
164 J. Park, J. Kim, Y. Yang, D. Yoon, H. Baik, S. Haam, H. Yang and K. Lee, *Adv. Sci.*, 2016, **3**, 1500252.
165 P. Anastas, N. Eghbali, V. Okatenko, A. Loiudice, M. A. Newton, D. C. Stoian, A. Blokhina, A. N. Chen, K. Rossi and R. Buonsanti, *Chem. Soc. Rev.*, 2010, **39**, 301–312.
166 Z. Li, Q. Xu, C. Yu, X. Guo, Z. Yin, Z. Zhao, X. Li, J. Robinson, M. Muzzio, C. J. Castilho, M. Shen, Y. Yuan, J. Wang, J. Antolik, G. Lu, D. Su, O. Chen, P. Guduru, C. T. Seto and S. Sun, *Matter*, 2017, **50**, 1449–1458.
167 D. Sun, V. Mazumder, Ö. Metin and S. Sun, *ACS Catal.*, 2016, **6**, 6892–6905.
168 S. Prodinger, M. F. K. Verstreken and R. F. Lobo, *ACS Sustainable Chem. Eng.*, 2020, **8**, 11930–11939.
169 Y. Song, K. Liu, S. Chen, L. Fan, C. Xia, P. Zhu, Y. Lu and H. Wang, *Nat. Commun.*, 2012, **11**, 3633.
170 Y. Yang, H. Xu, D. Cao, X. C. Zeng and D. Cheng, *ACS Catal.*, 2018, **9**, 781–790.
171 E. Doustkhah, M. Hasani, Y. Ide and M. H. N. Assadi, *ACS Appl. Nano Mater.*, 2020, **3**, 22–43.
172 S. Zhang, Ö. Metin, D. Su and S. Sun, *Angew. Chem., Int. Ed.*, 2013, **52**, 3681–3684.
173 B.-S. Choi, J. Song, M. Song, B. S. Goo, Y. W. Lee, Y. Kim, H. Yang and S. W. Han, *ACS Catal.*, 2019, **9**, 819–826.
174 J. Cheng, X. Gu, P. Liu, H. Zhang, L. Ma and H. Su, *Appl. Catal., B*, 2017, **218**, 460–469.
175 W.-Y. Yu, G. M. Mullen, D. W. Flaherty and C. B. Mullins, *J. Am. Chem. Soc.*, 2014, **136**, 11070–11078.
176 M. Karatok, H. T. Ngan, X. Jia, C. R. O'Connor, J. A. Boscoboinik, D. J. Stacchiola, P. Sautet and R. J. Madix, *J. Am. Chem. Soc.*, 2023, **145**, 5114–5124.
177 S. Akbayrak, S. Özkar, H. Kim, T. Y. Yoo, M. S. Bootharaju, J. H. Kim, D. Y. Chung and T. Hyeon, *Adv. Sci.*, 2018, **43**, 18592–18606.
178 D. Sun, V. Mazumder, Ö. Metin and S. Sun, *ACS Catal.*, 2012, **2**, 1290–1295.
179 T. A. A. Batchelor, J. K. Pedersen, S. H. Winther, I. E. Castelli, K. W. Jacobsen, J. Rossmeisl, Z. Zhao, C. Chen, Z. Liu, J. Huang, M. Wu, H. Liu, Y. Li and Y. Huang, *Catal. Sci. Technol.*, 2016, **6**, 6137–6143.
180 J. Li, S. M. Kathmann, H.-S. Hu, G. K. Schenter, T. Autrey and M. Gutowski, *Inorg. Chem.*, 2010, **49**, 7710–7720.
181 S. Özkar, *Chem. Mater.*, 2020, **45**, 7881–7891.
182 C. Yu, J. Fu, M. Muzzio, T. Shen, D. Su, J. Zhu and S. Sun, *Chem. Mater.*, 2017, **29**, 1413–1418.
183 X. Su and S. Li, *Int. J. Hydrogen Energy*, 2021, **46**, 14384–14394.
184 M. Muzzio, H. Lin, K. Wei, X. Guo, C. Yu, T. Yom, Z. Xi, Z. Yin and S. Sun, *ACS Sustainable Chem. Eng.*, 2020, **8**, 2814–2821.
185 X. Guo, C. Yu, Z. Yin, S. Sun and C. T. Seto, *ChemSusChem*, 2018, **11**, 1617–1620.
186 C. Yu, X. Guo, Z. Xi, M. Muzzio, Z. Yin, B. Shen, J. Li, C. T. Seto and S. Sun, *J. Am. Chem. Soc.*, 2017, **139**, 5712–5715.

187 S. Cheng, Y. Liu, Y. Zhao, X. Zhao, Z. Lang, H. Tan, T. Qiu and Y. Wang, *Dalton Trans.*, 2019, **48**, 17499–17506.
188 C. Yu, X. Guo, M. Shen, B. Shen, M. Muzzio, Z. Yin, Q. Li, Z. Xi, J. Li, C. T. Seto and S. Sun, *Angew. Chem., Int. Ed.*, 2017, **57**, 451–455.
189 Y. Liu, Q. Wang, L. Wu, Y. Long, J. Li, S. Song and H. Zhang, *Nanoscale*, 2019, **11**, 12932–12937.
190 C. Yu, X. Guo, B. Shen, Z. Xi, Q. Li, Z. Yin, H. Liu, M. Muzzio, M. Shen, J. Li, C. T. Seto and S. Sun, *J. Mater. Chem. A*, 2018, **6**, 23766–23772.
191 Z. Li, Q. Xu, C. Yu, X. Guo, Z. Yin, Z. Zhao, X. Li, J. Robinson, M. Muzzio, C. J. Castilho, M. Shen, Y. Yuan, J. Wang, J. Antolik, G. Lu, D. Su, O. Chen, P. Guduru, C. T. Seto and S. Sun, *Matter*, 2019, **1**, 1631–1643.
192 M. Shen, C. Yu, H. Guan, X. Dong, C. Harris, Z. Xiao, Z. Yin, M. Muzzio, H. Lin, J. R. Robinson, V. L. Colvin, S. Sun, K. Sun, T. Cheng, L. Wu, Y. Hu, J. Zhou, A. Maclennan, Z. Jiang, Y. Gao, W. A. Goddard and Z. Wang, *J. Am. Chem. Soc.*, 2021, **143**, 2115–2122.
193 M. Afshari, D. J. Sikkema, K. Lee and M. Bogle, *Polym. Rev.*, 2008, **48**, 230–274.
194 E. S. Park, J. Sieber, C. Guttman, K. Rice, K. Flynn, S. Watson and G. Holmes, *Anal. Chem.*, 2009, **81**, 9607–9617.
195 M. Shen, A. Afshar, N. Sinai, H. Guan, C. Harris, B. Rubenstein and S. Sun, *ACS Nano*, 2023, **18**, 178–185.
196 X. Li, P. Shen, Y. Luo, Y. Li, Y. Guo, H. Zhang and K. Chu, *Angew. Chem., Int. Ed.*, 2022, **134**, e202205923.
197 Q. Gao, B. Yao, H. S. Pillai, W. Zang, X. Han, Y. Liu, S.-W. Yu, Z. Yan, B. Min, S. Zhang, H. Zhou, L. Ma, H. Xin, Q. He and H. Zhu, *Nat. Synth.*, 2023, **2**, 624–634.
198 M. Xie, S. Tang, Z. Li, M. Wang, Z. Jin, P. Li, X. Zhan, H. Zhou and G. Yu, *J. Am. Chem. Soc.*, 2023, **145**, 13957–13967.

